Extension of finite volume compressible flow solvers to multi-dimensional, variable density zero Mach number flows

T. Schneider[†‡][1] and N. Botta[†‡][2] and K. J. Geratz[•] and R. Klein[†⊙‡]

[†] *Freie Universität Berlin, Mathematik und Informatik.*
[‡] *Konrad-Zuse-Zentrum für Informationstechnik Berlin.*
[•] *Institut für Technische Mechanik, RWTH Aachen.*
[⊙] *Potsdam Institute for Climate Impact Research.*

When attempting to compute unsteady, variable density flows at very small or zero Mach number using a standard finite volume compressible flow solver one faces at least the following difficulties: (i) Spatial pressure variations vanish as the Mach number $M \longrightarrow 0$, but they do affect the velocity field at leading order; (ii) the resulting spatial homogeneity of the leading order pressure implies an elliptic divergence constraint for the energy flux; (iii) violations of this constraint crucially affect the transport of mass, preventing a code to properly advect even a constant density distribution. We overcome these difficulties through a new algorithm for constructing numerical fluxes in the context of multi-dimensional finite volume methods in conservation form. The construction of numerical fluxes involves: (1) An explicit upwind step yielding predictions for the nonlinear convective flux components. (2) A first correction step that introduces pressure gradients which guarantee compliance of the convective fluxes with a divergence constraint. This step requires the solution of a first Poisson-type equation. (3) A second projection step which provides the yet unknown (non-convective) pressure contribution to the total flux of momentum. This second projection requires the solution of another Poisson-type equation and yields the cell centered velocity field at the new time. This velocity field exactly satisfies a divergence constraint consistent with the asymptotic limit. Step (1) can be done by any standard finite volume compressible flow solver. The input to steps (2) and (3) involves solely the fluxes from step (1) and is independent on how these were obtained. Thus, our approach allows any such solver to be extended to compute variable density incompressible flows.

Key Words: incompressible variable density flows; conservation laws

[1] Supported by the Deutsche Forschungsgemeinschaft under Contract KL611/5-1,2
[2] Supported by the Deutsche Forschungsgemeinschaft under Contract KL611/6-1

CONTENTS

1. INTRODUCTION

Low Mach number variable density flows play an important role in many natural and technological processes: Free convection in the atmosphere takes place at low speed and is controlled by the rate of change of density with height. The general circulation of the oceans is mainly driven by salinity and temperature, i.e. density, gradients. In combustion processes density fluctuations occur due to thermal gas expansion upon chemical energy conversion. If the flame fronts are thin in comparison with some characteristic length of the flow, these density fluctuations may have very steep gradients. Prominent examples are fuel/air combustors in energy plants, open fires, Otto engine combustion etc. Industrial processes like spray deposition and fluid jetting require the numerical simulation of fluids having different material properties. In these flows high density ratios (e.g. between water and air) and low velocities are common.

Numerical methods for low and zero Mach number flows couple the evolution in time of some set of dependent variables with *divergence constraints* for the underlying velocity fields. These constraints (e.g. $\nabla \cdot \vec{v} = 0$ in inviscid non reacting flows in closed domains of constant volume) arise because of the singularity of the governing equations in the limit of vanishing Mach number (M). Due to this singularity any numerical method for zero and low Mach number flows has to cope with at least two fundamental problems. These are the *dynamic range problem* and the *signal speed problem*. The dynamic range problem is associated with the fact that pressure fluctuations, non-dimensionalized by the background pressure, vanish as $M \longrightarrow 0$. As a consequence, their numerical representation deteriorates if only a single pressure variable is used in a numerical scheme. The signal speed problem arises from the order of magnitude difference between the speed of sound and a characteristic flow velocity as $M \longrightarrow 0$. The challenge is to operate a numerical scheme at time steps resolving *convection* processes, while still capturing correctly the net effects of acoustic waves. The dynamic range and the signal speed problem are manifestations of the fact that in the limit $M \longrightarrow 0$ the hyperbolic part of the governing equations degenerates to a mixed hyperbolic-elliptic operator. At zero Mach number a numerical formulation which explicitly accounts for the degeneration of the governing equations is unavoidable. In the regime of low but finite Mach numbers such formulation is necessary in order to overcome the accuracy and efficiency drawbacks which would affect a formulation which naively ignores the singularity of the limit $M \longrightarrow 0$.

In this paper attention is focused on the extension of conservative methods for compressible flows to the zero Mach number limit. Our approach is based on the low Mach number

asymptotic theory for conservation laws proposed in [19]. We show that the introduction of suitable elliptic constraints for the numerical fluxes of mass, momentum *and* energy allows any standard finite volume compressible flow solver to be used to compute zero Mach number flows. The fluxes are constrained via a semi-implicit procedure. First we compute an explicit approximation to the fluxes of an auxiliary hyperbolic system. In our implementation this is done in a predictor stage in which the influence of pressure gradients on the convective fluxes is neglected over a half time step. In the framework of e.g. Runge-Kutta schemes this step would simply reduce to a reconstruction step plus flux evaluation. Secondly a Poisson-type equation for cell-centered pressures is solved. This pressure allows the computation of convective fluxes of mass, momentum and energy that satisfy a velocity divergence constraint. Such constraint depends on the boundary conditions for the velocity field and on the source terms of the energy equation. At this point the grid cell interface pressure as a *non-convective* contribution to the momentum flux is yet unknown. This pressure is obtained by solving another suitable discrete form of the energy conservation law. This yields a second elliptic problem. The solution of this problem leads to a new cell-centered velocity field which *exactly* satisfies a discrete divergence constraint that is consistent with energy conservation.

The form of the auxiliary system associated with the computation of the convective fluxes is close to that of the compressible Euler equations but retains finite signal speeds as $M \longrightarrow 0$. Importantly, any finite volume compressible flow solver can be employed in this first explicit step after minor modifications. The overall scheme enjoys a CFL time step restriction which is dictated by the speed of the flow, is second order accurate on smooth flows and requires the solution of two elliptic problems per time step. The discrete operators associated with these problems have compact stencil. The resulting linear systems can be solved by standard iterative methods.

In the next two sections we discuss the relation between energy conservation and velocity divergence constraints in zero Mach number flows with variable density. We introduce an asymptotics based regularization and present a new approach for constructing fluxes via upwind techniques and divergence constraints that are consistent with energy conservation. Sections 4 and 5 describe in detail the construction of numerical fluxes. Section 6 deals with initial and boundary conditions for the explicit fluxes and for the elliptic problems. In this section we also discuss a time step restriction for our semi-implicit scheme. In section 7 we summarize the flux construction algorithm. To focus attention on the essentials of the method we consider inviscid non-reactive flows throughout the paper. At the end of section 3 we describe extensions of the method to account for viscosity, heat transfer and background compression/expansion and discuss the meaning of the first projection for Runge-Kutta time discretizations. In section 8 we point out the differences between the present and other modern approaches for the numerical computation of zero Mach number variable density flows. Numerical results are presented in section 9. We assess the accuracy of the method for unsteady constant as well as variable density flows. Numerical results for two and three dimensional inviscid flows are presented and discussed. We use standard driven cavity computations to validate a straightforward extension of the method to the viscous case and compare our results with reference solutions. In the last example we show the results of the numerical simulation of a thermo-acoustic refrigerator. This computation involves viscous effects, heat transfer and background compression/expansion. In the last section we draw conclusions and outline further work to be done.

2. DIVERGENCE CONSTRAINTS INDUCED BY ENERGY CONSERVATION

Consider the equations governing the evolution of a calorically perfect gas in a gravitational force field:

$$\begin{aligned}
&\rho_t + \nabla \cdot (\rho\vec{v}) = 0 \\
&(\rho\vec{v})_t + \nabla \cdot (\rho\vec{v} \circ \vec{v}) + \frac{1}{M^2}\nabla p = \frac{1}{Fr^2}\rho\vec{g} \\
&(\rho e)_t + \nabla \cdot ((\rho e + p)\vec{v}) = \frac{M^2}{Fr^2}\rho\vec{v}\cdot\vec{g} \\
&p = (\gamma - 1)(\rho e - \frac{1}{2}M^2\rho\vec{v}\cdot\vec{v})
\end{aligned} \tag{1}$$

γ represents the ratio of the specific heats which is assumed to be constant and set to 1.4 in all computation shown in this paper. By non-dimensionalization the acceleration $\vec{g}$ is a constant unit vector. In these equations all variables are dimensionless and $\mathcal{O}(1)$. M and Fr represent the Mach number and the Froude number respectively

$$M := \frac{u_{ref}}{\sqrt{p_{ref}/\rho_{ref}}} \quad Fr := \frac{u_{ref}}{\sqrt{g l_{ref}}}. \tag{2}$$

u_{ref}, p_{ref}, ρ_{ref} and l_{ref} are reference quantities and g is the (dimensional) acceleration due to gravity. For $M \longrightarrow 0$ the above equations develop a singularity, because:

1. The third term of the momentum equation $\nabla p/M^2$ obviously degenerates.
2. The eigenvalues of the Jacobian of the flux function $\mathbf{f}^M$ associated with the homogeneous part of (1)

$$\mathbf{f}^M := \begin{pmatrix} \rho\vec{v}\cdot\vec{n} \\ \rho\vec{v}\vec{v}\cdot\vec{n} + \frac{1}{M^2}p\vec{n} \\ (\rho e + p)\vec{v}\cdot\vec{n} \end{pmatrix} \tag{3}$$

degenerate as $M \longrightarrow 0$. These eigenvalues are $\vec{v}\cdot\vec{n}$ and $\vec{v}\cdot\vec{n} \pm c/M$ with $c^2 = \gamma p/\rho$ and $\vec{n}$ any unit vector.

Thus some reformulation is required. According to the asymptotic analysis presented in [34], [35], [19], we decompose the pressure p into a thermodynamic pressure $p^{(0)}$ and a second order pressure $p^{(2)}$ i.e. $p = p^{(0)} + M^2 p^{(2)}$. The leading order pressure $p^{(0)}$ is required to be homogeneous in space i.e. $\nabla p^{(0)} = 0$. As a result $\nabla p/M^2 = \nabla p^{(2)}$. With this formulation the governing equations for zero Mach number variable density flow in conservation form become

$$\begin{aligned}
&\rho_t + \nabla \cdot (\rho\vec{v}) = 0 \\
&(\rho\vec{v})_t + \nabla \cdot (\rho\vec{v} \circ \vec{v}) + \nabla p^{(2)} = \frac{1}{Fr^2}\rho\vec{g} \\
&(\rho e)_t + \nabla \cdot ((\rho e + p)\vec{v}) = 0 \\
&p = (\gamma - 1)\rho e \\
&p = p^{(0)}(t)
\end{aligned} \tag{4}$$

These are the equations we will deal with in this paper. We end this paragraph with the following three remarks, that are crucial for the subsequent developments:

Remark. Equation (4.5) and the state equation (4.4) imply a strong restriction on the energy ρe which must be prescribed at the initial time: this energy must be homogeneous in space.

Remark. Consider the zero Mach number governing equations (4). The rate of change of energy is

$$(\rho e)_t = \frac{1}{\gamma - 1} \frac{dp^{(0)}}{dt} \,. \tag{5}$$

If boundary conditions for the normal component of the velocity are prescribed on the boundary $\partial\Omega$ of the domain Ω:

$$\vec{v} \cdot \vec{n} = b \quad \text{on} \quad \partial\Omega \,, \tag{6}$$

then the rate of change of the thermodynamic pressure $p^{(0)}$ can be computed by integrating (4.3) over Ω, using equation (4.5), the state equation (4.4), the divergence theorem and the boundary condition (6)

$$|\Omega| \frac{dp^{(0)}}{dt} = -\gamma p^{(0)} \oint_{\partial\Omega} b \, dS \,. \tag{7}$$

Otherwise $dp^{(0)}/dt$ must be imposed and equation (7) is a constraint for the distribution of velocity along $\partial\Omega$. In both cases equation (5) implies a constraint for the energy flux, namely

$$\oint_{\partial V} (\rho e + p) \vec{v} \cdot \vec{n} \, dS = -|V| \frac{1}{\gamma - 1} \frac{dp^{(0)}}{dt} \tag{8}$$

for arbitrary $V \subset \Omega$. This is an integral constraint for the velocity divergence on V because $\rho e + p = \gamma/(\gamma - 1) p^{(0)}$ is constant in space.

Remark. The auxiliary system, (see [19])

$$\begin{aligned} &\rho_t + \nabla \cdot (\rho \vec{v}) = 0 \\ &(\rho \vec{v})_t + \nabla \cdot (\rho \vec{v} \circ \vec{v}) + \nabla p = \frac{1}{Fr^2} \rho \vec{g} \\ &(\rho e)_t + \nabla \cdot ((\rho e + p^{(0)}) \vec{v}) = 0 \\ &p = (\gamma - 1) \rho e \end{aligned} \tag{9}$$

with flux function

$$\mathbf{f}^* := \begin{pmatrix} \rho \vec{v} \cdot \vec{n} \\ \rho \vec{v} \vec{v} \cdot \vec{n} + p \vec{n} \\ (\rho e + p^{(0)}) \vec{v} \cdot \vec{n} \end{pmatrix} \tag{10}$$

enjoys the following properties:

1. The system is hyperbolic.

2. The eigenvalues of the Jacobian of the flux function $\mathbf{f}^*$ are $\vec{v}\cdot\vec{n}$ and $\vec{v}\cdot\vec{n} \pm c$ with $c^2 := (\gamma-1)(\rho e + p^{(0)})/\rho$ (see [19]).

3. This system has the same convective fluxes as the zero Mach number governing equations (4).

4. Solutions of (9) satisfy, for homogeneous pressure p and zero flow divergence at time $t = 0$, the following estimates at time $t > 0$ (see appendix A.1):

$$\begin{aligned} \nabla \cdot \vec{v} &= \mathcal{O}(t) \\ \nabla p &= \mathcal{O}(t^2)\,. \end{aligned} \tag{11}$$

System (9) is the auxiliary hyperbolic system mentioned earlier, which is used in the first step of our method to obtain explicit predictions of the convective fluxes.

3. FLUX CONSTRUCTION

Consider a finite volume method for the zero Mach number governing equations (4):

$$\mathbf{U}_V^{n+1} = \mathbf{U}_V^n - \frac{\delta t}{|V|} \sum_{I \in \mathcal{I}_{\partial V}} |I|\, \mathbf{F}_I + \delta t \mathbf{W}_V\,. \tag{12}$$

$\mathbf{U}_V^n$ is a numerical approximation to the average $\mathbf{u}_V^n$ of the solution $\mathbf{u}(\vec{x},t)$ of (4) over the cell V at time t^n

$$\mathbf{U}_V^n \approx \mathbf{u}_V^n \qquad \mathbf{u}_V^n := \frac{1}{|V|}\int_V \mathbf{u}(\vec{x},t^n)\,dV \qquad \mathbf{u} := \begin{pmatrix} \rho \\ \rho\vec{v} \\ \rho e \end{pmatrix}. \tag{13}$$

$\mathbf{F}_I$ and $\mathbf{W}_V$ are numerical approximations to the averages $\mathbf{f}_I$ and $\mathbf{w}_V$ of the flux function $\mathbf{f}$ and of the right hand side $\mathbf{w}$ of (4). These averages are taken over the time interval $[t^n, t^{n+1} := t^n + \delta t]$ and over the interface I and the cell V for $\mathbf{f}_I$ and $\mathbf{w}_V$, respectively.

$$\mathbf{F}_I \approx \mathbf{f}_I \quad \mathbf{f}_I := \frac{1}{\delta t}\frac{1}{|I|}\int_{t^n}^{t^{n+1}}\int_I \mathbf{f}(\mathbf{u}(\vec{x},t),\vec{n}(\vec{x}))\,dS\,dt \qquad \mathbf{f} := \begin{pmatrix} \rho\vec{v}\cdot\vec{n} \\ \rho\vec{v}\vec{v}\cdot\vec{n} + p^{(2)}\vec{n} \\ (\rho e + p)\vec{v}\cdot\vec{n} \end{pmatrix} \tag{14}$$

$$\mathbf{W}_V \approx \mathbf{w}_V \qquad \mathbf{w}_V := \frac{1}{\delta t}\frac{1}{|V|}\int_{t^n}^{t^{n+1}}\int_V \mathbf{w}(\mathbf{u}(\vec{x},t))\,dV\,dt \qquad \mathbf{w} := \begin{pmatrix} 0 \\ \frac{1}{Fr^2}\rho\vec{g} \\ 0 \end{pmatrix}. \tag{15}$$

V is a cell of a conformal space discretization of Ω. $|V|$ is the volume of V. I is an interface between two adjacent cells and $|I|$ is the area of I. By $\mathcal{V}, \mathcal{I}$ we denote the set of all cells and of all interfaces, respectively. $\mathcal{I}_{\partial V} \subset \mathcal{I}$ are those interfaces of $\mathcal{I}$ which lay on the boundary ∂V of the cell V. The sum on the right hand side of (12) is equivalent to the double integral on $[t^n, t^{n+1}] \times \partial V$

$$\delta t \sum_{I \in \mathcal{I}_{\partial V}} |I|\, \mathbf{f}_I = \int_{t^n}^{t^{n+1}} \oint_{\partial V} \mathbf{f}\,dS\,dt\,. \tag{16}$$

We use the indices $\mathcal{V}$ and $\mathcal{I}$ to represent sets of cell and interface averages, respectively. In particular $\mathbf{U}^n_{\mathcal{V}}$ is a set of approximate cell averages (space averages) at time t^n while $\mathbf{F}_{\mathcal{I}}$, $\mathbf{W}_{\mathcal{V}}$ represent sets of interface and cell averages (space and time averages). The time averages are taken over the interval $[t^n, t^{n+1}]$. We will often use the term *numerical flux* to indicate an interface average $\mathbf{F}_I$. In our implementation the space discretization is a regular Cartesian grid in two or three space dimensions, but we expect our approach to be applicable to more complex spatial discretizations as well. We focus the attention on second order schemes.

We propose a new algorithm for constructing numerical fluxes $\mathbf{F}_{\mathcal{I}}$ for the finite volume method (12). These are defined through the flux function $\mathbf{f}$ as follows

$$\mathbf{F}_I := \mathbf{f}(\mathbf{U}_I, \vec{n}_I) = \begin{pmatrix} \rho\vec{v}\cdot\vec{n} \\ \rho\vec{v}\vec{v}\cdot\vec{n} + p^{(2)}\vec{n} \\ \rho h\vec{v}\cdot\vec{n} \end{pmatrix}_I . \tag{17}$$

In (17) the enthalpy $\rho h := \rho e + p$ has been used to express the energy flux. The numerical fluxes or, equivalently, the interface averages $\mathbf{U}_{\mathcal{I}}$, are constructed according to the following criteria

1. $\mathbf{F}_I$ is defined on the basis of higher order upwind rules with respect to convection.

2. The interface average velocities $\vec{v}_{\mathcal{I}}$ used to construct the numerical fluxes $\mathbf{F}_{\mathcal{I}}$ satisfy the divergence constraint (8), thereby guaranteeing energy conservation.

3. On smooth solutions $\mathbf{F}_I$ approximates the average flux $\mathbf{f}_I$ up to errors of order $\mathcal{O}(\delta t^2)$.

The numerical fluxes are obtained as follows. First explicit auxiliary numerical fluxes $\mathbf{F}^*_{\mathcal{I}}$ are computed

$$\mathbf{F}^*_I := \begin{pmatrix} \rho\vec{v}\cdot\vec{n} \\ \rho\vec{v}\vec{v}\cdot\vec{n} + p\vec{n} \\ \rho h^0\vec{v}\cdot\vec{n} \end{pmatrix}^*_I \tag{18}$$

with $h^{(0)} := e + p^{(0)}/\rho$. $\mathbf{F}^*_I$ approximates the average flux $\mathbf{f}^*_I$

$$\mathbf{F}^*_I \approx \mathbf{f}^*_I \qquad \mathbf{f}^*_I := \frac{1}{\delta t}\frac{1}{|I|}\int_{t^n}^{t^{n+1}}\int_I \mathbf{f}^*(\mathbf{u}(\vec{x},t), \vec{n}(\vec{x}))\, dS\, dt \tag{19}$$

of the auxiliary system (9) up to errors of order $\mathcal{O}(\delta t^2)$. The auxiliary numerical fluxes are computed by using an explicit high resolution upwind method for hyperbolic systems of conservation laws. Our present implementation employs operator splitting techniques to account for the source terms. The high resolution method is a MUSCL scheme (see [22], [23], [24], [25], [26]) based on slope limiting of characteristic variables and the numerical flux proposed by *Einfeldt* [12]. This flux has been extended for system (9) according to the characteristic analysis presented in [19].

Once $\mathbf{F}^*_{\mathcal{I}}$ are known we apply a two-step elliptic correction to compute the final numerical fluxes $\mathbf{F}_{\mathcal{I}}$. In the first step we compute the *convective part* of $\mathbf{F}_{\mathcal{I}}$. In particular, the interface velocities $\vec{v}^*_{\mathcal{I}}$ associated with the auxiliary numerical flux $\mathbf{F}^*_{\mathcal{I}}$ are corrected to enforce the

divergence constraint (8):

$$\vec{v}_I = \vec{v}_I^* - \frac{\delta t}{2}\frac{\nabla p^{(2)}|_I}{\rho_I} \qquad \forall\, I \in \mathcal{I} \tag{20}$$

$$\sum_{I \in \mathcal{I}_{\partial V}} |I|\,(\rho h \vec{v})_I \cdot \vec{n}_I = -|V|\frac{1}{\gamma - 1}\frac{dp^{(0)}}{dt} \qquad \forall\, V \in \mathcal{V}. \tag{21}$$

Notice that the correction term on the right hand side of (20) can be interpreted as a numerical approximation for the integral over $I \times [t^n, t^n + \delta t/2]$ of the difference between the acceleration implied by the governing equations (4) and that implied by the auxiliary system (9). The estimate (11.2) guarantees that this interpretation is correct up to terms of order $\mathcal{O}(\delta t^3)$. Assume the interface averages ρ_I, h_I are known. Then equations (20),(21) are, in conjunction with a linear rule to compute $\nabla p^{(2)}|_I$ on the basis of cell-centered pressures $p_\mathcal{V}^{(2)}$, a discrete Poisson-type problem for these pressures. Its solution provides $p_\mathcal{V}^{(2)}$ and the interface average velocity $\vec{v}_I$ responsible for advecting mass, momentum and energy. The pressure gradient $\nabla p^{(2)}|_I$ guarantees, through (21), that these interface velocities satisfy the divergence constraint associated with energy conservation. This is a crucial property in conservative schemes for zero Mach number variable density flows: a violation of this property implies, e.g., the failure to properly advect even a constant density distribution! This first step closely resembles a MAC projection as described in [16]. In the present context it naturally follows from energy conservation.

In the second correction step the pressure component of the momentum flux at the interfaces, $p_I^{(2)}\vec{n}_I$ is computed. A straightforward way to do this would be to use the cell-centered values $p_\mathcal{V}^{(2)}$ to compute, e.g. by the trapezoidal rule, the interface average pressures. This simple approach, however, does *not* guarantee that the new velocities $\vec{v}_\mathcal{V}^{n+1}$ exactly satisfy the zero Mach number divergence constraints. To enforce this property the pressure forces $p_I^{(2)}\vec{n}_I$ are computed by solving a second Poisson-type problem. This problem is discussed in section 5.

In summary our scheme is a systematic procedure for constructing numerical approximations to the interface averages of $\mathbf{f}$ over $I \times [t^n, t^n + \delta t]$. Consistently with second order accuracy, the time integrals are replaced by δt times second order approximations to the exact values of the integrand at time $t = t^n + \delta t/2$. These approximations are defined in terms of three contributions: the explicit flux $\mathbf{F}_I^*$ yields the influence of convection on the time evolution of ρ, $\rho\vec{v}$ and ρe. The first correction step includes the effect of $\nabla p^{(2)}$ on the interface velocities. Finally, the second projection provides the pressure contribution $p^{(2)}$ to the momentum flux at the desired time level.

There is a conceptually different interpretation of this construction of numerical fluxes for (4). One may view the scheme as an add-on to an existing explicit compressible flow solver. The sophisticated technology of a high resolution scheme is employed to provide proper upwinding for the convective fluxes, thereby allowing a robust representation of high Reynolds number or even inviscid flows.

In this context the two correction steps can be understood as discrete projections for the intermediate interface velocity field $\vec{v}_\mathcal{I}$ and for the final cell velocity field $\vec{v}_\mathcal{V}^{n+1}$. These projections are similar in spirit to Chorin's original projection method from [10], [9] and more recent advanced schemes, e.g., in [2], [3], [33], [13], [1].

3.1. Extensions of the method

Viscous flows. The method outlined in the last two sections can be easily extended to to cope with viscous flows. A model with zero heat conduction and finite Reynolds (Re) number has been used in the computation of the driven cavity flows presented in section 9. At zero Mach number viscosity has no effect on the energy balance (because the work of viscous forces scales with M^2/Re) and only enters in the momentum equation through a viscous stress

$$\frac{1}{Re}\nabla\cdot\tau \qquad \tau := \nabla\vec{v} + (\nabla\vec{v})^T - \frac{2}{3}\nabla\cdot\vec{v} \tag{22}$$

on the right hand side of the zero Mach number governing equations (4.2) and of the auxiliary system (9.2). In the finite volume method viscous effects appear in the form of a numerical viscous flux; equation (12) becomes

$$\mathbf{U}_V^{n+1} = \mathbf{U}_V^n - \frac{\delta t}{|V|}\sum_{I\in\mathcal{I}_{\partial V}} |I|\,\mathbf{F}_I + \frac{\delta t}{|V|}\sum_{I\in\mathcal{I}_{\partial V}} |I|\,\mathbf{R}_I + \delta t\mathbf{W}_V\,.$$

$$\mathbf{R}_I \approx \mathbf{r}_I \quad \mathbf{r}_I := \frac{1}{\delta t}\frac{1}{|I|}\int_{t^n}^{t^{n+1}}\!\!\int_I \mathbf{r}(\mathbf{u}(\vec{x},t),\vec{n}(\vec{x}))\,dS\,dt \qquad \mathbf{r} := \begin{pmatrix} 0 \\ \frac{1}{Re}\tau\cdot\vec{n} \\ 0 \end{pmatrix}$$

In the extended method such fluxes are added to the convective fluxes e.g. via *Strang* [38] splitting.

Heat transfer, background compression/expansion. Heat conduction brings an additional term on the right hand side of the energy equation:

$$\frac{\gamma}{\gamma-1}\frac{1}{PrRe}\nabla\cdot\nabla T\,. \tag{23}$$

Pr and T denote the Prandtl number and the temperature, respectively. The thermal conductivity is assumed to be constant. Let

$$\nabla T\cdot\vec{n} = q \quad \text{on} \quad \partial\Omega \tag{24}$$

be the boundary condition for the heat flux across the boundary $\partial\Omega$ of the domain Ω. The additional term modifies the divergence constraint that results from energy conservation. The rate of change of the thermodynamic pressure $p^{(0)}$ becomes

$$|\Omega|\frac{dp^{(0)}}{dt} = -\gamma p^{(0)}\oint_{\partial\Omega} b\,dS + \gamma\frac{1}{PrRe}\oint_{\partial\Omega} q\,dS\,. \tag{25}$$

The divergence constraint (8) for the velocity on some arbitrary $V\subset\Omega$ becomes local; using the equation of state $p^{(0)} = \rho T$ for the temperature T this constraint can be written as

$$\oint_{\partial V}(\rho e + p)\vec{v}\cdot\vec{n}\,dS = -|V|\frac{1}{\gamma-1}\frac{dp^{(0)}}{dt} + \frac{\gamma}{\gamma-1}\frac{p^{(0)}}{PrRe}\oint_{\partial V}\nabla\left(\frac{1}{\rho}\right)\cdot\vec{n}\,dS\,. \tag{26}$$

The first term on the right hand side of (26) is determined by equation (25). In the computation with heat transfer to be presented in section 9 the time step integration is done with a second order Runge-Kutta scheme:

$$\begin{aligned}
\mathbf{U}_V^{n+\frac{1}{2}} &= \mathbf{U}_V^n - \frac{\delta t}{2|V|} \sum_{I \in \mathcal{I}_{\partial V}} |I| \left(\mathbf{F}_I^n + \mathbf{R}_I^n + \mathbf{Q}_I^n\right) \\
\mathbf{U}_V^{n+1} &= \mathbf{U}_V^n - \frac{\delta t}{|V|} \sum_{I \in \mathcal{I}_{\partial V}} |I| \left(\mathbf{F}_I^{n+\frac{1}{2}} + \mathbf{R}_I^{n+\frac{1}{2}} + \mathbf{Q}_I^{n+\frac{1}{2}}\right)
\end{aligned}$$

$$\mathbf{Q}_I^n \approx \mathbf{q}_I^n \quad \mathbf{q}_I^n := \frac{1}{|I|} \int_I \mathbf{q}(\mathbf{u}(\vec{x}, t^n), \vec{n}(\vec{x}))\, dS \quad \mathbf{q} := \begin{pmatrix} 0 \\ 0 \\ \frac{\gamma}{\gamma - 1} \frac{p^{(0)}}{PrRe} \nabla \left(\frac{1}{\rho}\right) \cdot \vec{n} \end{pmatrix}$$

In the above scheme the numerical fluxes $\mathbf{F}_I^n$, $\mathbf{F}_I^{n+\frac{1}{2}}$, $\mathbf{R}_I^n$ and $\mathbf{R}_I^{n+\frac{1}{2}}$ do not represent time averages. As the heat fluxes $\mathbf{Q}_I^n$, $\mathbf{Q}_I^{n+\frac{1}{2}}$, they are evaluated at fixed times. In the computation of the numerical fluxes the cell interface pressure $p_I^{(2)}$ is approximated by the pressure that results from the first projection. This is done in order to restrict the number of elliptic problems per time step to two. The order of the method is not affected by this approximation.

4. CONVECTIVE FLUXES

In this section the algorithm for computing the convective part of the numerical fluxes $\mathbf{F}_\mathcal{I}$, i.e. the interface averages $\rho_I \vec{v}_I \cdot \vec{n}_I$, $\rho_I \vec{v}_I \vec{v}_I \cdot \vec{n}_I$ and $\rho_I h_I \vec{v}_I \cdot \vec{n}_I$ in (17), is described in detail. We assume that the auxiliary numerical fluxes $\mathbf{F}_\mathcal{I}^*$ are known. As explained in the introduction $\mathbf{F}_\mathcal{I}^*$ are computed by a standard high resolution method for the auxiliary system (9). $\mathbf{F}_\mathcal{I}$ are then constructed according to the following rules:

1. Density ρ_I and enthalpy h_I are those associated with the numerical flux $\mathbf{F}_I^*$:

$$\begin{aligned}
\rho_I &= \rho_I^* \\
h_I &= h_I^{0,*}.
\end{aligned} \tag{27}$$

2. The velocity $\vec{v}_I$ is obtained from $\vec{v}_I^*$ through the projection step (20), (21).

Using these rules and the definition of $\mathbf{F}_I^*$ in (18) we find

$$\mathbf{F}_I = \mathbf{F}_I^* - \frac{\delta t}{2} \begin{pmatrix} \nabla p^{(2)} \cdot \vec{n} \\ \vec{v}^* \nabla p^{(2)} \cdot \vec{n} + \nabla p^{(2)} \vec{v}^* \cdot \vec{n} - p^{(2)} \vec{n} \\ h^{0,*} \nabla p^{(2)} \cdot \vec{n} \end{pmatrix}_I \tag{28}$$

up to terms $\mathcal{O}(\delta t^2)$. As mentioned in the introduction, the pressure gradient $\nabla p^{(2)}|_I$ is computed on the basis of cell-centered pressures $p_\mathcal{V}^{(2)}$. Let

$$\nabla p^{(2)}|_I := G_\mathcal{I}^\mathcal{V}(p_\mathcal{V}^{(2)})|_I = G_I^\mathcal{V}(p_\mathcal{V}^{(2)}). \tag{29}$$

$G_\mathcal{I}^\mathcal{V}(p_\mathcal{V}^{(2)})$ is a linear operator mapping cell-centered pressures into interface average pressure gradients. Using (29) and (27) the discrete Poisson-type problem (20), (21) for the cell-

centered pressures $p_{\mathcal{V}}^{(2)}$ becomes

$$\frac{\delta t}{2} \sum_{I \in \mathcal{I}_{\partial V}} |I| \, h_I^{0,*} G_I^{\mathcal{V}}(p_{\mathcal{V}}^{(2)}) \cdot \vec{n}_I = \sum_{I \in \mathcal{I}_{\partial V}} |I| \, (\rho h^0 \vec{v})_I^* \cdot \vec{n}_I + \frac{|V|}{\gamma - 1} \frac{dp^{(0)}}{dt} \qquad \forall V \in \mathcal{V} \,. \quad (30)$$

Let $D_{\mathcal{V}}^{\mathcal{I}}$ be the discrete divergence

$$D_{\mathcal{V}}^{\mathcal{I}}(\cdot): \quad D_{\mathcal{V}}^{\mathcal{I}}(\vec{a}_{\mathcal{I}})|_V = D_V^{\mathcal{I}}(\vec{a}_{\mathcal{I}}) := \frac{1}{|V|} \sum_{I \in \mathcal{I}_{\partial V}} |I| \, \vec{a}_I \cdot \vec{n}_I \qquad \forall V \in \mathcal{V} \,. \quad (31)$$

$D_{\mathcal{V}}^{\mathcal{I}}$ maps interface averages of vector fields into their cell average divergences. Using $G_{\mathcal{I}}^{\mathcal{V}}$, $D_{\mathcal{V}}^{\mathcal{I}}$ the linear system (30) for the cell-centered pressures $p_{\mathcal{V}}^{(2)}$ reads

$$\frac{\delta t}{2} D_{\mathcal{V}}^{\mathcal{I}} \left(h_{\mathcal{I}}^{0,*} G_{\mathcal{I}}^{\mathcal{V}} \left(p_{\mathcal{V}}^{(2)} \right) \right) = D_{\mathcal{V}}^{\mathcal{I}} \left((\rho h^0 \vec{v})_{\mathcal{I}}^* \right) + \frac{1}{\gamma - 1} \frac{dp^{(0)}}{dt} \,. \quad (32)$$

The set product appearing as the argument of the discrete divergence operator on the left hand side of (32) is the set of interface averages, say $\vec{w}_{\mathcal{I}}^*$ such that $\vec{w}_I^* := h_I^{0,*} G_I^{\mathcal{V}}(p_{\mathcal{V}}^{(2)})$. The gradient $G_{\mathcal{I}}^{\mathcal{V}}$ is defined in such a way that the discrete Laplacian on the left hand side of (32) has compact stencil and the linear system for $p_{\mathcal{V}}^{(2)}$ can be solved by standard iterative methods. With $G_{\mathcal{I}}^{\mathcal{V}}$ as given in appendix A.2, $D_{\mathcal{V}}^{\mathcal{I}} G_{\mathcal{I}}^{\mathcal{V}}$ is, on Cartesian grids, the standard 5-point (7-point) Laplacian in two (three) space dimensions. Boundary conditions for (32) are discussed in section 6.

Notice that our flux construction algorithm (28) requires, besides the auxiliary flux $\mathbf{F}_{\mathcal{I}}^*$, the interface averages $\rho_{\mathcal{I}}^*$, $\vec{v}_{\mathcal{I}}^*$ and $h_{\mathcal{I}}^{0,*}$. The enthalpy $h_{\mathcal{I}}^{0,*}$ also appears in the elliptic problem (32) for the pressures $p_{\mathcal{V}}^{(2)}$. This is a delicate issue, because the numerical flux $\mathbf{F}_I^*$ is not obtained, in general, by evaluating the exact flux function $\mathbf{f}^*$ in some state $\mathbf{U}_I$. After all, as explained in the introduction, we do not want to restrict the computation of $\mathbf{F}_{\mathcal{I}}^*$ to some special class of high resolution methods. In our current implementation, for instance, $\mathbf{F}_{\mathcal{I}}^*$ are computed using a standard high resolution method which makes use of directional splitting and approximate Riemann problem solvers, but any other method designed for the hyperbolic system (9) could be used as well. We circumvent this problem by computing $\rho_{\mathcal{I}}^*$ (and $\vec{v}_{\mathcal{I}}^*$, $h_{\mathcal{I}}^{0,*}$) through a suitable interpolation of cell averages

$$\rho_{\mathcal{I}}^* := L_{\mathcal{I}}^{\mathcal{V}} \left(\rho_{\mathcal{V}}^* \right) \,. \quad (33)$$

The cell averages $\rho_{\mathcal{V}}^*$ are those obtained by advancing the data from time level t^n to time level $t^n + \delta t$ using the high resolution finite volume method for the auxiliary system (9).

5. INTERFACE PRESSURES

Consider the finite volume method (12). With the convective fluxes for mass and energy computed as described in the previous section, this method provides the cell averages $\rho_{\mathcal{V}}^{n+1}$ and $(\rho e)_{\mathcal{V}}^{n+1}$ at the new time t^{n+1}. Due to our exact projection

$$(\rho e)_V^{n+1} = \frac{1}{\gamma - 1} p^{(0)}(t^{n+1}) \qquad \forall V \in \mathcal{V} \,. \quad (34)$$

To compute the new cell averages $(\rho\vec{v})_V^{n+1}$ we still need the pressure components of the momentum flux: this is the last term of (14.2). Let

$$(\rho\vec{v})_V^{n+1} = (\rho\vec{v})_V^{**} - \frac{\delta t}{|V|}\sum_{I\in\mathcal{I}_{\partial V}} |I|\, p_I^{(2)}\,\vec{n}_I\,. \tag{35}$$

Here $(\rho\vec{v})_V^{**}$ is the cell average obtained by setting $p_I^{(2)}$ to zero in the momentum flux (28.2) while retaining the effects of $\nabla p^{(2)}\cdot\vec{n}$ on $\rho\vec{v}\vec{v}\cdot\vec{n}$ and using the finite volume method (12) to update $(\rho\vec{v})_V^n$. Remember that $p_I^{(2)}$ is, according to (14), a numerical approximation to the average, on $[t^n, t^{n+1}]\times I$, of the exact pressure $p^{(2)}$. Assume a numerical approximation to the exact pressure $p^{(2)}$ at time $t^n + \delta t/2$ be known in the grid nodes. Then the interface average $p_I^{(2)}$ could be computed from the nodal values using some suitable quadrature rule.

We need to extend our notation: let $\overline{\mathcal{V}}$ be a *dual* discretization of Ω. $\overline{\mathcal{V}}$ consists of control volumes $\overline{V}$ centered around the nodes of the original grid. The interfaces between the cells of $\overline{\mathcal{V}}$ are denoted by $\overline{I}$. As usual $\overline{\mathcal{I}}$ is the set of all such interfaces. In figure 1 a cell-centered and a node-centered control volume, V and $\overline{V}$, are drawn for a two dimensional Cartesian grid. In this figure the cell centers, the nodes and the midpoints of the interfaces are marked by circles, squares and crosses, respectively. Let $p_{\overline{\mathcal{V}}}^{(2)}$ be a set of node-centered pressures.

FIG. 1. Cell (V) and node centered ($\overline{V}$) control volumes; cell centers, nodes and the midpoints of the interfaces are marked by circles, squares and crosses, respectively.

The interface-centered pressures $p_{\mathcal{I}}^{(2)}$ can be computed by

$$p_{\mathcal{I}}^{(2)} := L_{\mathcal{I}}^{\overline{\mathcal{V}}}\left(p_{\overline{\mathcal{V}}}^{(2)}\right)\,. \tag{36}$$

In (36) $L_{\mathcal{I}}^{\overline{\mathcal{V}}}$ is a linear operator which maps nodal values into interface averages. Let $G_{\mathcal{V}}^{\overline{\mathcal{V}}}$ be the linear operator

$$G_{\mathcal{V}}^{\overline{\mathcal{V}}}(\cdot): \quad G_{\mathcal{V}}^{\overline{\mathcal{V}}}(a_{\overline{\mathcal{V}}})\big|_V = G_V^{\overline{\mathcal{V}}}(a_{\overline{\mathcal{V}}}) := \frac{1}{|V|}\sum_{I\in\mathcal{I}_{\partial V}} |I|\, L_I^{\overline{\mathcal{V}}}(a_{\overline{\mathcal{V}}})\,\vec{n}_I \tag{37}$$

mapping nodal values of a scalar a into cell averages of its gradient field. Using (36) and (37), the last step of our finite volume method for the momentum equation reads

$$(\rho\vec{v})_V^{n+1} = (\rho\vec{v})_V^{**} - \delta t G_V^{\overline{\mathcal{V}}}\left(p_{\overline{\mathcal{V}}}^{(2)}\right)\,. \tag{38}$$

The nodal values $p_{\overline{\mathcal{V}}}^{(2)}$ are computed following an idea originally proposed by *Geratz* [18]. The average change of energy on $\overline{V}$:

$$(\rho e)_{\overline{V}}^{n+1} - (\rho e)_{\overline{V}}^{n} := -\frac{\delta t}{|\overline{V}|}\sum_{\overline{I}\in\overline{\mathcal{I}}_{\partial\overline{V}}} |\overline{I}|\,\frac{1}{2}((\rho h\vec{v})_{\overline{I}}^{n} + (\rho h\vec{v})_{\overline{I}}^{n+1})\cdot\vec{n}_{\overline{I}} \tag{39}$$

is required to be consistent with the constraint (5) i.e.

$$(\rho e)_{\overline{V}}^{n+1} - (\rho e)_{\overline{V}}^{n} = \frac{1}{\gamma-1}\left(p^{(0),n+1} - p^{(0),n}\right)\,. \tag{40}$$

$p^{(0),n+1}$ is the same as was computed and used in the first projection step. Notice that the interface averages under the sum on the right hand side of (39) can be expressed to the desired order accuracy by means of cell averages:

$$(\rho h\vec{v})^n_{\mathcal{I}} = L^{\mathcal{V}}_{\mathcal{I}}\left((\rho h\vec{v})^n_{\mathcal{V}}\right) . \tag{41}$$

$L^{\mathcal{V}}_{\mathcal{I}}$ is a (linear) operator mapping cell averages into interface averages. The interfaces are those associated with the control volumes of the dual grid. In fact (39) is a finite volume method for the averages of (ρe) on the cells of the dual grid and the sum on the right hand side of (39) is, after division by $|\overline{V}|$, a discrete divergence. Let $D^{\mathcal{V}}_{\overline{\mathcal{V}}}$ be *this* discrete divergence:

$$D^{\mathcal{V}}_{\overline{\mathcal{V}}}(\cdot): \quad D^{\mathcal{V}}_{\overline{\mathcal{V}}}(\vec{a}_{\mathcal{V}})|_{\overline{V}} \;=\; D^{\mathcal{V}}_{\overline{\mathcal{V}}}(\vec{a}_{\mathcal{V}}) \;:=\; \frac{1}{|\overline{V}|}\sum_{\overline{I}\in\overline{\mathcal{I}}_{\partial\overline{V}}} |\overline{I}|\, L^{\mathcal{V}}_{\mathcal{I}}(\vec{a}_{\mathcal{V}})\cdot\vec{n}_{\overline{I}}\,. \tag{42}$$

Using $L^{\mathcal{V}}_{\mathcal{I}}$, $D^{\mathcal{V}}_{\overline{\mathcal{V}}}$ and taking into account equation (40) the finite volume method (39) yields

$$-\delta t D^{\mathcal{V}}_{\overline{\mathcal{V}}}((\rho h\vec{v})^{n+1}_{\mathcal{V}}) \;=\; \delta t D^{\mathcal{V}}_{\overline{\mathcal{V}}}((\rho h\vec{v})^n_{\mathcal{V}}) + \frac{2}{\gamma-1}\left(p^{(0),n+1}-p^{(0),n}\right) . \tag{43}$$

Using equation (38) to replace the new cell averages $(\rho h\vec{v})^{n+1}_{\mathcal{V}}$ on the left hand side of this equation leads to the following elliptic problem for the unknown nodal pressures $p^{(2)}_{\overline{\mathcal{V}}}$:

$$\begin{aligned}\delta t D^{\mathcal{V}}_{\overline{\mathcal{V}}}\left(h^{n+1}_{\mathcal{V}} G^{\overline{\mathcal{V}}}_{\mathcal{V}}\left(p^{(2)}_{\overline{\mathcal{V}}}\right)\right) \;&=\; D^{\mathcal{V}}_{\overline{\mathcal{V}}}(h^{n+1}_{\mathcal{V}}(\rho\vec{v})^{**}_{\mathcal{V}}) + D^{\mathcal{V}}_{\overline{\mathcal{V}}}((\rho h\vec{v})^n_{\mathcal{V}}) \\ &+\; \frac{2}{\gamma-1}\frac{p^{(0),n+1}-p^{(0),n}}{\delta t}\,.\end{aligned} \tag{44}$$

The linear operators $L^{\mathcal{V}}_{\mathcal{I}}$ and $L^{\overline{\mathcal{V}}}_{\mathcal{I}}$ are chosen in such a way that the discrete Laplacian $D^{\mathcal{V}}_{\overline{\mathcal{V}}}G^{\overline{\mathcal{V}}}_{\mathcal{V}}$ has a compact stencil and the linear system (44) for $p^{(2)}_{\overline{\mathcal{V}}}$ can be solved by standard iterative methods. Boundary conditions for (44) are discussed in section 6; the explicit rules for computing $G^{\overline{\mathcal{V}}}_{\mathcal{V}}$ and $D^{\mathcal{V}}_{\overline{\mathcal{V}}}$ on Cartesian grids that we have used to produce the results shown in section 9 are given in appendix A.3. For flows without background compression or expansion the last term on the right hand side of (44) is zero. In this case the new velocities

$$\vec{v}^{n+1}_{\mathcal{V}}: \quad \vec{v}^{n+1}_{V} := (\rho\vec{v})^{n+1}_{V}/\rho^{n+1}_{V} \tag{45}$$

are divergence free in the following sense.

LEMMA 5.1. *Let $D^{\mathcal{V}}_{\overline{\mathcal{V}}}(\vec{v}^n_{\mathcal{V}})=0$, $(\rho h)^n_{\mathcal{V}}$ homogeneous in space and $p^{(0),n+1}=p^{(0),n}$ (no background compression or expansion). Then $(\rho e)^{n+1}_{\mathcal{V}}$ are homogeneous in space and the velocities $\vec{v}^{n+1}_{\mathcal{V}}$ obtained by our semi-implicit fluxes from (38) where $p^{(2)}_{\overline{\mathcal{V}}}$ is solution of (44) satisfy $D^{\mathcal{V}}_{\overline{\mathcal{V}}}(\vec{v}^{n+1}_{\mathcal{V}})=0$.*

Proof of Lemma 5.1. For $p^{(0),n+1}=p^{(0),n}$ equation (44) becomes

$$\delta t D^{\mathcal{V}}_{\overline{\mathcal{V}}}\left(\frac{(\rho h)^{n+1}_{\mathcal{V}}}{\rho^{n+1}_{\mathcal{V}}}G^{\overline{\mathcal{V}}}_{\mathcal{V}}\left(p^{(2)}_{\overline{\mathcal{V}}}\right)\right) - D^{\mathcal{V}}_{\overline{\mathcal{V}}}\left(\frac{(\rho h)^{n+1}_{\mathcal{V}}}{\rho^{n+1}_{\mathcal{V}}}(\rho\vec{v})^{**}_{\mathcal{V}}\right) - D^{\mathcal{V}}_{\overline{\mathcal{V}}}((\rho h)^n_{\mathcal{V}}\vec{v}^n_{\mathcal{V}}) = 0. \tag{46}$$

Remember that our flux correction method has been constructed around a divergence constraint that guarantees the new cell averages $(\rho e)^{n+1}_{\mathcal{V}}$ to be homogeneous in space (cf.

equation (34)). Therefore $(\rho h)_{\mathcal{V}}^{n+1}$ are homogeneous in space as well. Using homogeneity of $(\rho h)_{\mathcal{V}}^{n}$, $(\rho h)_{\mathcal{V}}^{n+1}$, the linearity of $D_{\mathcal{V}}^{\mathcal{V}}$ and the assumption $D_{\mathcal{V}}^{\mathcal{V}}(\vec{v}_{\mathcal{V}}^{n}) = 0$ equation (46) yields

$$D_{\mathcal{V}}^{\mathcal{V}}\left(\frac{1}{\rho_{\mathcal{V}}^{n+1}}\left(\rho\vec{v}_{\mathcal{V}}^{**} - \delta t G_{\mathcal{V}}^{\overline{\mathcal{V}}}\left(p_{\overline{\mathcal{V}}}^{(2)}\right)\right)\right) = D_{\mathcal{V}}^{\mathcal{V}}\left(\frac{1}{\rho_{\mathcal{V}}^{n+1}}(\rho\vec{v})_{\mathcal{V}}^{n+1}\right) = D_{\mathcal{V}}^{\mathcal{V}}(\vec{v}_{\mathcal{V}}^{n+1}) = 0.$$

Remark. Notice: In the last two sections we have formulated the details of the method in a general fashion to support readers interested in applying our approach to curvilinear or unstructured grids. Specialized formulae for Cartesian grids are compiled in appendices A.2 and A.3.

6. INITIAL AND BOUNDARY CONDITIONS; TIME STEP RESTRICTION

In this section we discuss initial conditions for the approximate cell averages at time $t = 0$ and boundary conditions for the computation of the auxiliary numerical flux $\mathbf{F}_{\mathcal{I}}^{*}$ and for the Poisson equations (32) and (44). We also address the problem of finding a suitable time step restriction for our semi-implicit method.

6.1. Initial conditions

As mentioned in the introduction the constraint $\nabla p^{(0)} = 0$ implies, because of the state equation (4), a restriction on the initial condition for the energy (ρe), namely

$$\nabla(\rho e) = 0.$$

The initial cell averages $(\rho e)_{V}^{0}$ must be homogeneous in space and equal to $p^{(0)}(0)/(\gamma - 1)$. We take $p^{(0)}(0) = 1$. The initial density distribution is arbitrary. In section 9 we show numerical results both for smooth and for discontinuous density distributions. In the case of a falling "droplet", for instance, the density is equal to 1000 inside the droplet and 1 outside. The initial velocity field

$$\vec{v}_{V}^{0} := \frac{(\rho\vec{v})_{V}^{0}}{\rho_{V}^{0}}$$

is required to satisfy the divergence constraint

$$D_{\overline{V}}^{\mathcal{V}}(\vec{v}_{\mathcal{V}}^{0}) = \frac{1}{\gamma p^{(0)}}\left.\frac{dp^{(0)}}{dt}\right|_{t=0} \qquad \forall\,\overline{V} \in \overline{\mathcal{V}}.$$

As stated in Lemma 5.1 $D_{\mathcal{V}}^{\mathcal{V}}(\vec{v}_{\mathcal{V}}^{0}) = 0$ is sufficient, for constant background pressure $p^{(0)}$, to obtain $D_{\mathcal{V}}^{\mathcal{V}}(\vec{v}_{\mathcal{V}}^{n}) = 0$ for all $n > 0$. Using an argument similar to the proof of Lemma 5.1 one can show that this condition is also necessary.

6.2. Boundary conditions

In a finite volume formulation boundary conditions appear as constraints for the numerical fluxes on $\partial\Omega$. In our method the interface averages $\mathbf{F}_{\mathcal{I}}$ are computed by means of an implicit correction of the explicit auxiliary numerical fluxes $\mathbf{F}_{\mathcal{I}}^{*}$. Thus, we have to prescribe boundary conditions both for $\mathbf{F}_{\mathcal{I}}^{*}$ and for the implicit cell-centered and node-centered pressures $p^{(2)}$.

6.2.1. Explicit fluxes

For periodic boundary conditions the constraints for $\mathbf{F}^*_{\mathcal{I}}$ are straightforward. For rigid non permeable walls the convective part of $\mathbf{F}_I$ must be zero. This constraint applies to the numerical flux $\mathbf{F}^*_I$ as well:

$$\mathbf{F}^*_I := \begin{pmatrix} 0 \\ p\vec{n} \\ 0 \end{pmatrix}^*_I \qquad \forall\, I \in \mathcal{I}_w. \tag{47}$$

In the above equation $\mathcal{I}_w$ represents the set of all wall interfaces. Boundary conditions for in- and outflow boundaries can be derived by coupling suitable assumptions about the outside of the computational domain with a characteristic analysis of the governing equations. Again these boundary conditions must be translated into constraints for the numerical fluxes $\mathbf{F}^*_{\mathcal{I}}$.

In our Cartesian grid framework the boundary conditions are implemented by filling rows of "ghost" cells laying outside the computational domain with suitable cell averages and then treating $\partial\Omega$ as a set of standard grid cell interfaces. In the case of periodic boundary conditions the rules for filling these cells are straightforward. Let V be a ghost cell and V' the image obtained reflecting V with respect to the boundary. Let $I' \in \mathcal{I}_w$ be the boundary interface lying between V and V'. For rigid non permeable fixed walls one can show that, with the numerical flux function that we use to compute $\mathbf{F}^*_{I'}$, the filling rules

$$\begin{aligned} \rho_V &= \rho_{V'} \\ \vec{v}_V \cdot \vec{n} &= -\vec{v}_{V'} \cdot \vec{n} \\ p_V &= p_{V'} \end{aligned}$$

are sufficient to guarantee that the numerical flux $\mathbf{F}^*_{I'}$ satisfies the boundary conditions (47). In the case of inflow and outflow boundaries other filling rules must be derived. Notice that, in general, the filling rules depend both on the boundary conditions and on the numerical flux function used to construct $\mathbf{F}^*_{\mathcal{I}}$. Notice also that, no matter what the boundary condition, the energy flux $F^*_{\rho e,\mathcal{I}}$ on $\partial\Omega$ must satisfy some discrete form of the integral condition (7). As we will see in the next paragraph this is a solvability constraint for the elliptic problem (32) for the cell-centered pressures $p^{(2)}_{\mathcal{V}}$.

6.2.2. Cell centered pressures.

Consider the Poisson-type problem associated with the first projection, equation (32). The normal derivative

$$\nabla p^{(2)}\big|_I \cdot \vec{n}_I := G^{\mathcal{V}}_I\,(p^{(2)}_{\mathcal{V}}) \cdot \vec{n}_I$$

must be evaluated on all interfaces belonging to the boundary $\partial\Omega$ of the computational domain. Let the boundary condition for the auxiliary interface velocity $\vec{v}^*_I$ be the same as those for $\vec{v}_I$ i.e.

$$\vec{v}^*_I \cdot \vec{n}_I = \vec{v}_I \cdot \vec{n}_I\,. \tag{48}$$

This assumption seems to be quite standard in projection methods and has been used in all our computations. Using (48) equation (20) yields

$$\frac{\delta t}{2}\frac{1}{\rho_I}G_I^{\mathcal{V}}(p_{\mathcal{V}}^{(2)})\cdot\vec{n}_I = (\vec{v}_I^{\,*}-\vec{v}_I)\cdot\vec{n}_I = 0 \qquad \forall\, I\subset\partial\Omega.$$

With these boundary conditions the right hand side of the linear system (32) must satisfy an integral constraint for a solution $p_{\mathcal{V}}^{(2)}$ to exist, namely:

$$\sum_{V\in\mathcal{V}}|V|D_V^{\mathcal{I}}\left(\vec{F}^{\,*}_{\rho e,\mathcal{I}}\right)+\frac{|\Omega|}{\gamma-1}\frac{dp^{(0)}}{dt}=0 \tag{49}$$

Notice that (49) is nothing but a discrete form of equation (7) which prescribes the rate of change of the background pressure $p^{(0)}$ on the basis of the mass flux through the boundary $\partial\Omega$ of the computational domain. Equation (7) was directly derived from the governing equations for zero Mach number flows (4). In the introduction we pointed out that $dp^{(0)}/dt$ must be computed from (7) or, alternatively, that (7) implies, for a given $dp^{(0)}/dt$ an integral constraint for the velocities on $\partial\Omega$. However we did not specify in which discrete sense equation (7) should be fulfilled: the answer to this question is now given by equation (49).

6.2.3. Node centered pressures.

Consider the elliptic problem (44) for the nodal pressures $p_{\overline{\mathcal{V}}}^{(2)}$. To compute the divergence field $D_{\overline{\mathcal{V}}}^{\mathcal{V}}$ the discrete normal derivative

$$L_{\overline{\mathcal{I}}}^{\mathcal{V}}\left(h_{\mathcal{V}}^{n+1}G_{\mathcal{V}}^{\overline{\mathcal{V}}}\left(p_{\overline{\mathcal{V}}}^{(2)}\right)\right)\cdot\vec{n}_{\overline{I}}$$

and the scalar products

$$L_{\overline{\mathcal{I}}}^{\mathcal{V}}\left(h_{\mathcal{V}}^{n+1}(\rho\vec{v})_{\mathcal{V}}^{**}\right)\cdot\vec{n}_{\overline{I}} \qquad L_{\overline{\mathcal{I}}}^{\mathcal{V}}\left((\rho h\vec{v})_{\mathcal{V}}^{n}\right)\cdot\vec{n}_{\overline{I}} \tag{50}$$

must be evaluated on interfaces $\overline{I}\in\overline{\mathcal{I}}$ laying beyond the boundary of the computational domain Ω. This has been done as follows. The dual cells around nodes laying on walls of $\partial\Omega$ have been cut by $\partial\Omega$: on these interfaces both the normal derivative of $p_{\overline{\mathcal{V}}}^{(2)}$ and the scalar products (50) have been set to zero. Dual cells around nodes laying on periodic boundaries have been left overlap the outside of Ω: rows of "ghost" cell averages and nodes have been filled with suitable values and $L_{\overline{\mathcal{I}}}^{\mathcal{V}}$ has been evaluated as on internal interfaces.

6.3. Time step restriction

Because of the explicit computation of the numerical fluxes $\mathbf{F}_I^*$, the time step δt is subject to a CFL [31] stability restriction. We use $\delta t := C\delta t^*$ with $0\le C<1$ and

$$\delta t^* := \min_{I\in\mathcal{I}}\left\{\frac{1}{|I|}\min\left\{\frac{|V_I^L|}{|\min\{0,\vec{v}_I^{\,*}\cdot\vec{n}_I-c_I^*\}|},\frac{|V_I^R|}{\max\{0,\vec{v}_I^{\,*}\cdot\vec{n}_I+c_I^*\}}\right\}\right\}.$$

V_I^L, V_I^R are the control volumes on the two sides of the I-interface. Notice that on a regular grid of spacing δx this restriction implies $\delta t = C\mathcal{O}(\delta x)$ because the characteristic speeds $\vec{v}\cdot\vec{n}\pm c$ of the auxiliary system (9) are of $\mathcal{O}(1)$. C is a safety factor. In most of the computations presented in section 9 we used $C=0.8$.

7. SUMMARY OF THE TIME STEP ALGORITHM

In this section we summarize the time step algorithm for the computation of the approximate cell averages $\mathbf{U}_{\mathcal{V}}^{n+1}$ at time $t^{n+1} := t^n + \delta t$ from $\mathbf{U}_{\mathcal{V}}^n$. The time step δt is given by the constraint from section 6.3. We assume that the boundary conditions are compatible with the background pressure $p^{(0)}(t)$ (in the sense that suitable discrete forms of (7) e.g. equation (49), hold) and that cell averages of ghost cells are properly set whenever they are needed.

1. **Explicit numerical fluxes and interface averages.** Using a standard high resolution finite volume method for the auxiliary system (9) compute numerical fluxes $\mathbf{F}_{\mathcal{I}}^*$, source terms $\mathbf{W}_{\mathcal{V}}^*$ and auxiliary cell averages

$$\mathbf{U}_V^* := \mathbf{U}_V^n - \frac{\delta t}{|V|} \sum_{I \in \mathcal{I}_{\partial V}} |I|\, \mathbf{F}_I^* + \delta t \mathbf{W}_V^* \,. \tag{51}$$

Compute the auxiliary interface averages

$$\rho_{\mathcal{I}}^* := L_{\mathcal{I}}^{\mathcal{V}}\left(\rho_{\mathcal{V}}^*\right) \qquad \vec{v}_{\mathcal{I}}^* := L_{\mathcal{I}}^{\mathcal{V}}\left(\vec{v}_{\mathcal{V}}^*\right) \qquad h_{\mathcal{I}}^{0,*} := L_{\mathcal{I}}^{\mathcal{V}}\left(h_{\mathcal{V}}^{0,*}\right) .$$

2. **Implicit flux correction: cell-centered pressures.** Solve the discrete Poisson problem for the cell-centered pressures $p_{\mathcal{V}}^{(2)}$:

$$\frac{\delta t}{2} D_{\mathcal{V}}^{\mathcal{I}}\left(h_{\mathcal{I}}^{0,*} G_{\mathcal{I}}^{\mathcal{V}}\left(p_{\mathcal{V}}^{(2)}\right)\right) = D_{\mathcal{V}}^{\mathcal{I}}\left(\left(\rho h^0 \vec{v}\right)_I^*\right) + \frac{1}{\gamma - 1}\frac{dp^{(0)}}{dt}$$

3. **Implicit flux correction: density and energy updates, source term.** Compute the numerical fluxes of density and energy

$$F_{\rho,I} = F_{\rho,I}^* - \frac{\delta t}{2} G_I^{\mathcal{V}}\left(p_{\mathcal{V}}^{(2)}\right) \cdot \vec{n}_I \qquad F_{\rho e,I} = F_{\rho e,I}^* - \frac{\delta t}{2} h_I^{0,*} G_I^{\mathcal{V}}\left(p_{\mathcal{V}}^{(2)}\right) \cdot \vec{n}_I \,,$$

the new density and energy cell averages

$$\rho_V^{n+1} = \rho_V^n - \frac{\delta t}{|V|} \sum_{I \in \mathcal{I}_{\partial V}} |I|\, F_{\rho,I} \qquad (\rho e)_V^{n+1} = (\rho e)_V^n - \frac{\delta t}{|V|} \sum_{I \in \mathcal{I}_{\partial V}} |I|\, F_{\rho e,I},$$

and the source term of the momentum equation

$$W_{\rho \vec{v},V} := \frac{1}{Fr^2}\frac{1}{2}\left(\rho_V^n + \rho_V^{n+1}\right)\vec{g}$$

4. **Implicit flux correction: intermediate momentum update.** Compute the convective momentum numerical fluxes

$$F_{\rho\vec{v},I}^{**} = F_{\rho\vec{v},I}^* - \frac{\delta t}{2}\left(\vec{v}_I^* G_I^{\mathcal{V}}\left(p_{\mathcal{V}}^{(2)}\right) \cdot \vec{n}_I + G_I^{\mathcal{V}}\left(p_{\mathcal{V}}^{(2)}\right) \vec{v}_I^* \cdot \vec{n}_I\right),$$

and the temporary momentum cell averages

$$\rho\vec{v}_V^{**} = \rho\vec{v}_V^n - \frac{\delta t}{|V|} \sum_{I \in \mathcal{I}_{\partial V}} |I|\, F_{\rho\vec{v},I}^{**} + \delta t W_{\rho\vec{v},V} \tag{52}$$

5. **Implicit flux correction: node-centered pressures.** Solve the discrete Poisson problem for the node-centered pressures $p_{\overline{\mathcal{V}}}^{(2)}$:

$$\delta t D_{\overline{\mathcal{V}}}^{\mathcal{V}}\left(h_{\mathcal{V}}^{n+1} G_{\mathcal{V}}^{\overline{\mathcal{V}}}\left(p_{\overline{\mathcal{V}}}^{(2)}\right)\right) = D_{\overline{\mathcal{V}}}^{\mathcal{V}}\left(h_{\mathcal{V}}^{n+1}(\rho\vec{v})_{\mathcal{V}}^{**}\right) + D_{\overline{\mathcal{V}}}^{\mathcal{V}}\left((\rho h\vec{v})_{\mathcal{V}}^{n}\right) + \frac{2}{\gamma-1}\frac{p^{(0),n+1}-p^{(0),n}}{\delta t}\,.$$

6. **Implicit flux correction: final momentum update.** Compute the new cell averages

$$(\rho\vec{v})_{V}^{n+1} = (\rho\vec{v})_{V}^{**} - \delta t G_{V}^{\overline{\mathcal{V}}}\left(p_{\overline{\mathcal{V}}}^{(2)}\right)\,.$$

Remark. Note that the combination of the intermediate and final momentum updates are equivalent to the following formulation of the effective momentum flux

$$F_{\rho\vec{v},I} = F_{\rho\vec{v},I}^{**} + \left(p_I^{(2)} - p^{(0),n+1/2}\right)\cdot\vec{n}_I \qquad p_I^{(2)} = L_I^{\overline{\mathcal{V}}}\left(p_{\overline{\mathcal{V}}}^{(2)}\right)$$

Remark. In the present implementation $\mathbf{F}_{\mathcal{I}}^{*}$ and $\mathbf{W}_{\mathcal{V}}^{*}$ are computed by coupling a standard high resolution finite volume method for hyperbolic systems of conservation laws with *Strang* [38] splitting to account for the source term on the right hand side of the auxiliary system (9):

$$\begin{aligned}
\mathbf{U}_{V}^{n,1} &:= \mathbf{U}_{V}^{n} - \frac{\delta t}{2}\frac{1}{|V|}\sum_{I\in\mathcal{I}_{\partial V}}|I|\,\mathbf{F}_{I}^{*}\left(\mathbf{U}_{\mathcal{V}}^{n}\right)\\
\mathbf{U}_{V}^{n,2} &:= \mathbf{U}_{V}^{n,1} + \delta t\mathbf{W}_{V}^{*}\left(\mathbf{U}_{\mathcal{V}}^{n,1}\right)\\
\mathbf{U}_{V}^{*} &:= \mathbf{U}_{V}^{n,2} - \frac{\delta t}{2}\frac{1}{|V|}\sum_{I\in\mathcal{I}_{\partial V}}|I|\,\mathbf{F}_{I}^{*}\left(\mathbf{U}_{\mathcal{V}}^{n,2}\right)
\end{aligned} \tag{53}$$

Steps $(53)_1$, $(53)_3$ and $(53)_2$ are second order numerical methods for the homogeneous part and for the source term of (9), respectively:

$$\begin{aligned}
\rho_t + \nabla\cdot(\rho\vec{v}) &= 0 & \rho_t &= 0\\
(\rho\vec{v})_t + \nabla\cdot(\rho\vec{v}\circ\vec{v}) + \nabla p &= 0 & (\rho\vec{v})_t &= \frac{1}{Fr^2}\rho\vec{g}\\
(\rho e)_t + \nabla\cdot((\rho e + p^{(0)})\vec{v}) &= 0 & (\rho e)_t &= 0\,.
\end{aligned} \tag{54}$$

Comparing (53) with (51) yields

$$\mathbf{F}_{I}^{*} = \frac{1}{2}\left(\mathbf{F}_{I}^{*}\left(\mathbf{U}_{\mathcal{V}}^{n}\right) + \mathbf{F}_{I}^{*}\left(\mathbf{U}_{\mathcal{V}}^{n,2}\right)\right) \qquad \mathbf{W}_{V}^{*} = \mathbf{W}_{V}^{*}\left(\mathbf{U}_{\mathcal{V}}^{n,1}\right) \tag{55}$$

8. RELATION TO OTHER LOW AND ZERO MACH NUMBER APPROACHES

Projection methods. The present method resembles a projection method for incompressible flows [10], [9], [2], [3], [33] in that we first generate *explicit* estimates for various vector fields which are then corrected in an additional elliptic projection step so as to comply with the desired divergence constraints. Our scheme differs from these techniques in various ways, however:

1. Chorin's classical projection method and its modern higher order extensions explicitly adopt a constraint for the velocity divergence. Their "projection step" thus projects explicit estimates of the velocity field back onto the subspace of divergence-free fields or onto the subspace of fields with a prescribed divergence in more general situations. In contrast, the first elliptic correction in our conservative finite volume scheme yields *convective fluxes* that are consistent with energy conservation for zero Mach number. In this fashion we combine projection techniques with the conservation of mass, momentum and energy.

2. The projection step of a projection method is an abstract mathematical construction designed to achieve velocity fields complying with suitable divergence constraints and the pressure is validly considered as a "Lagrangian multiplier" in this context. In contrast, the first elliptic flux correction in our scheme naturally appears as part of a half-timestep update from time level t^n to $t^n + \delta t/2$ of the convective fluxes at grid cell-interfaces based on the original equations.

3. Most of the projection methods cited require a single elliptic solve per time step. Our approach requires two, which are in addition based on two different discretizations of the Poisson operator in the respective pressure equations.

4. On the other hand, our approach does not compromise on the discrete divergence, which we satisfy exactly up to the order of the convergence threshold of our elliptic solvers. Thus we avoid the approximate projection that has been introduced in a number of higher order projection methods.

SIMPLE-type methods. Extensions of incompressible flow solvers for inclusion of compressibility effects are often based on the SIMPLE [39] method for incompressible flows of *Karki* & *Patankar* [5]. Successful representative examples of this class of methods can be found in [14], [17], [7].

One important feature of these methods is also implemented in our approach: There is a separate scaling of the background pressure by some suitable thermodynamic reference value and of pressure gradients or pressure corrections by a characteristic value of $\rho|\vec{v}|^2$. This is equivalent to the introduction of two separate pressure variables in the sense of an asymptotic expansion $p = p^{(0)}(t) + M^2 p^{(2)}(\vec{x}, t)$ with a spatially homogeneous leading order pressure (notice that $M^2 \sim \rho|\vec{v}|^2/p$ in dimensional variables). We have also found this kind of "multiple pressure variable ansatz" to be a necessary ingredient of a numerical method that is supposed to smoothly transit to zero Mach number (see the later sections and [19], [8]).

In [8] the authors also discuss the compressibility extension of a class of SIMPLE-type methods and provide a more comprehensive account of earlier work in this area. Their work goes beyond earlier approaches in that they explicitly allow for the presence of acoustic pulses that are compatible with the small Mach number assumption, but nevertheless affect the velocity field at leading order. The abovementioned pressure expansion $p = p^{(0)} + M^2 p^{(2)}$ with $\nabla p^{(0)} \equiv 0$ precludes such a leading order acoustic effect. This is, in fact, common knowledge from the theory of characteristics [32], has been proven rigorously in [34], [35] and was discussed in the context of a multiple length scales asymptotic expansion in [19]. Thus, in [8] the authors introduce a three-fold pressure expansion $p = p^{(0)} + M p^{(1)} + M^2 p^{(2)}$ in the SIMPLE framework and include a physics-induced multi-grid procedure in order to deal with long wavelength acoustics associated with $p^{(1)}$. There are currently two major differences between these derivatives of incompressible flow computation methods and the approach proposed in this paper:

1. Some of the SIMPLE-type schemes are able to handle flows with large *spatial* variations of the local flow Mach number [17], [14].

2. The SIMPLE-type schemes generally compromise on conservation of one or more of the fundamental conserved quantities, mass, momentum and energy.

The first item emphasizes a current limitation of our approach, as we assume a single, spatially global characteristic Mach number. The asymptotic analysis that backs up our numerical techniques will have to be extended in future work to include this case, which is important for quite a number of realistic applications. As a consequence of the second item, the extended SIMPLE schemes do not automatically reduce to a conservative finite volume formulation for compressible flows as the Mach number increases. This, on the other hand, was one of the major motivations of the present work, even though in this paper we only discuss the zero Mach number limit version of our method (see [18] for a first "all Mach number implementation" in more than one space dimension).

Direct extensions of high resolution shock capturing schemes. Another class of low Mach number techniques results from the desire to extend existing modern high resolution shock capturing schemes to the incompressible limit. This is also one of the key points of the present paper. In [20], [21], [6], [15] the truncation and round-off errors of various compressible flow solvers are carefully analyzed in the limit of small Mach numbers. The approach in [20], [21] differs quite substantially from that in [6], [15] but both arrive at the same conclusion: The incompressible limit cannot be achieved by standard compressible flow solvers, unless particular care is taken to eliminate large errors that stem from subtle interactions of truncation errors and the zero Mach number singularity of the compressible flow equations.

The difficulties of representing low Mach number flows are traced back in [21] to round-off errors upon subtraction of large numbers. This is consistent with the previous discussions regarding the asymptotic pressure scaling $p = p^{(0)}(t) + M^2 p^{(2)}(\vec{x}, t)$. As $M \longrightarrow 0$, spatial pressure differences are of order $O(M^2)$ and naive discrete differentiation of p without an appropriate rescaling must ultimately result in unacceptable round-off errors. Interestingly, the authors in [21] do not introduce this scaling explicitly as, e.g., in [17], [14], [19], [8], [18]. Instead they propose to let the automatic scaling of modern floating point arithmetic take care of the problem. The idea is to always handle deviations from appropriately chosen homogeneous background values rather than the original absolute values of all flow quantities. The reader should consult the original references regarding a detailed account of differentiation schemes that do not suffer from the round-off error problem. It is not clear to us, whether the approach actually allows to compute the limit for $M = 0$, because (i) the floating point arithmetic would have to overcome an infinite gap in amplitudes and (ii) there is no evidence that the numerical solutions obey, for Mach number tending to zero, a proper divergence constraint.

The ansatz in [6], [15] specifically addresses higher order upwind schemes that can be written in the form of central differences plus the effects of an upwind dissipation matrix. One prominent example is Roe's method. Turkel's [11] pre conditioning technique, originally developed only for steady state computations, is employed and selectively applied only to the upwind dissipation terms. It is shown that artificially excited small scale acoustics that are associated with $O(M)$ pressure variations can be suppressed in this fashion. In contrast to the original method in [11] the resulting scheme does provide a consistent discretization of the unsteady flow equations. Unfortunately, the authors do not

provide any evidence that their numerical solutions would actually approach a divergence-free flow as the Mach number diminishes and that their pressure variables obey some elliptic Poisson-type equation. By employing an implicit time stepping algorithm, the dissipation-preconditioned scheme does not suffer from the sound-speed CFL constraint, so that efficient computations are possible even for very small Mach numbers.

9. NUMERICAL RESULTS

In this section we discuss the numerical results obtained with the semi-implicit method for five test problems. The first four problems are chosen to assess the accuracy and the efficiency of the method and test its capability to cope with large density variations and small scale gravity driven flows. For these tests either the exact solution or at least some properties of the exact solution are known. This allows a meaningful validation of the method and provides a flavor of the difficulties that must be faced in the numerical simulation of more realistic flows. Problem number five is included to show that the proposed numerical method can be extended to cope with boundary driven backward compression/expansion, viscous forces and heat transfer. All test problems can be run with trivial geometries. For the first five problems the boundary conditions are those discussed in section 6. These imply a constant thermodynamic pressure $p^{(0)}$. Thus $dp^{(0)}/dt = 0$ and $p^{(0),n} = p^{(0),0}$ $\forall n \geq 0$.

The computations have been performed on regular Cartesian grids. The discrete gradient and divergence operators and the linear systems for the cell-centered and for the node-centered pressures are those explicitly given in appendixes A.2 and A.3. These two linear systems must be solved at each time step. This has been done using a multi-grid preconditioned conjugate gradient method. The difference with respect to the standard conjugate gradient solver is that, in each iteration, the new residual vector is computed by applying a multi-grid cycle to the previous residual vector. There are several ways of visiting the grid levels during the multi-grid procedure, such as a V-cycle, W-cycle, F-cycle [30] and nested cycle. In our case, the F-cycle turned out to provide the best contraction rate. As smoother a Gauss-Seidel method was used with two pre and post smoothing steps on each grid level. In two space dimensions a standard nine point prolongation operator was used. This operator is defined through bilinear interpolation. In three dimensions trilinear interpolation provides a 27 point prolongation operator. The adjoint prolongation operator served as restriction operator. In presence of large density variations, the coefficients of both linear systems can change by order of magnitudes. In this case the linear coarse grid operators need to be constructed by Galerkin's approximation [30].

As expected the computations show that the CPU time needed to solve the systems depends linearly on the number of unknowns. The solution of the linear systems accounts for about 95% of the time required for a computation and demands a memory allocation of roughly one K-byte per computational point. In each solution the residuals

$$r_2(p_{\mathcal{V}}^{(2)}) := \left\| D_{\mathcal{V}}^{\mathcal{I}}\left((\rho h^0 \vec{v})_{\mathcal{I}}^*\right) - \frac{\delta t}{2} D_{\mathcal{V}}^{\mathcal{I}}\left(h_{\mathcal{I}}^{0,*} G_{\mathcal{I}}^{\mathcal{V}}\left(p_{\mathcal{V}}^{(2)}\right)\right) \right\|_2$$

$$r_2(p_{\overline{\mathcal{V}}}^{(2)}) := \left\| D_{\overline{\mathcal{V}}}^{\mathcal{V}}\left(h_{\mathcal{V}}^{n+1}(\rho\vec{v})_{\mathcal{V}}^{**}\right) + D_{\overline{\mathcal{V}}}^{\mathcal{V}}\left((\rho h\vec{v})_{\mathcal{V}}^{n}\right) - \delta t D_{\overline{\mathcal{V}}}^{\mathcal{V}}\left(h_{\mathcal{V}}^{n+1} G_{\mathcal{V}}^{\overline{\mathcal{V}}}\left(p_{\overline{\mathcal{V}}}^{(2)}\right)\right)\right\|_2$$

have been driven down to 10^{-7}. In the above definitions $\|a_{\mathcal{V}}\|_2$ represents the Euclidean norm of a vector whose components are the values $a_{\mathcal{V}}$ i.e.

$$\|a_{\mathcal{V}}\|_2 := \left(\sum_{V \in \mathcal{V}} a_V^2 \right)^{1/2}$$

and similarly for $\|a_{\overline{\mathcal{V}}}\|_2$.

9.1. Convergence studies.

This test problem was originally proposed in *Almgren et al.* [33]. It has been designed to assess the accuracy of the method on constant density flows. For any time t and $0 < x < 1$, $0 < y < 1$, the velocity field

$$\begin{aligned} u(x,y,t) :=& 1 - 2\cos(2\pi(x-t))\sin(2\pi(y-t)) \\ v(x,y,t) :=& 1 + 2\sin(2\pi(x-t))\cos(2\pi(y-t)), \end{aligned}$$

together with the pressure $p^{(2)}(x,y,t)$

$$p^{(2)}(x,y,t) := -\cos(4\pi(x-t)) - \cos(4\pi(y-t))$$

is an exact solution of the zero Mach number governing equations (4) with constant pressure $p(x,y,t)$, constant density $\rho(x,y,t)$ and periodic boundary conditions on the unit square. Starting from $t = 0$, we have computed numerical approximations $u_{i,j}^N$ to the cell-averages $u(x_i, y_j, t^N)$ of the exact velocity u at time $t^N = 3$. Similarly $v_{i,j}^N$, $\rho_{i,j}^N$ are numerical approximations to the cell-averages $v(x_i, y_j, t^N)$ and $\rho(x_i, y_j, t^N)$ of the exact v, ρ at time $t^N = 3$.

Three equally spaced regular Cartesian grids of spacings $h = 1/32$, $h = 1/64$ and $h = 1/128$ have been used on the unit square. On a each grid the time step was chosen according to a fixed Courant number $C = 0.8$. (see section 6.3). The initial cell averages $(\rho\vec{v})_{i,j}^0$ have been computed for $\vec{v}_{i,j}^0$ to be discretely divergence free

$$(\rho\vec{v})_{i,j}^0 = (\rho\vec{v})(x_i, y_j, 0) - G_{i,j}^{\overline{\mathcal{V}}}\left(p_{\overline{\mathcal{V}}}^{(2),0}\right)$$

i.e the initial pressure $p_{\overline{\mathcal{V}}}^{(2),0}$ is solution of the Poisson problem

$$D_{\overline{\mathcal{V}}}^{\mathcal{V}}\left(\frac{1}{\rho_{i,j}^0} G_{i,j}^{\overline{\mathcal{V}}}\left(p_{\overline{\mathcal{V}}}^{(2),0}\right)\right) = D_{\overline{\mathcal{V}}}^{\mathcal{V}}\left(\frac{(\rho\vec{v})(x_i, y_j, 0)}{\rho_{i,j}^0}\right)$$

with $\rho_{i,j}^0 = \rho(x_i, y_j, 0) = 1$. In the MUSCL scheme for the computation of the auxiliary numerical fluxes $\mathbf{F}_{\mathcal{I}}^*$ unlimited slopes have been used. For each grid we have measured the 2-norm e_2 and the maximum norm e_∞ of the cell-error $e_{i,j}$ at time $t^N = 3$:

$$e_{i,j} := \left|\rho(x_i, y_j, t^N) - \rho_{i,j}^N\right| + \left|u(x_i, y_j, t^N) - u_{i,j}^N\right| + \left|v(x_i, y_j, t^N) - v_{i,j}^N\right|.$$

$$e_2 := \left(\sum_{i,j} (e_{i,j} h)^2 \right)^{1/2} \qquad e_\infty := \max_{i,j} \{e_{i,j}\}$$

Notice that this is essentially a measure of the velocity error: due to the exact projection of the interface velocity, the density error in the 2-norm is of the same order as $r_2(p_\nu^{(2)})$ i.e. 10^{-7}. Table 1 shows e_2, e_∞ on the three grids together with the corresponding convergence rates. These have been computed as follows: Given e.g. coarse and fine grid 2-norm

TABLE 1

Constant density: errors and convergence rates in the 2-norm and in the maximum norm.

errors $e_{2,c}$, $e_{2,f}$ and the corresponding grid spacings h_c, h_f the convergence rate p is

$$p := \frac{\log(e_{2,c}/e_{2,f})}{\log(h_c/h_f)}$$

The exact velocity field (9.1) has been constructed by differentiating the streamline function

$$\phi(x,y,t) := y - x + \frac{1}{\pi}\cos(2\pi(x-t))\cos(2\pi(y-t))$$

and taking $u := \partial\phi/\partial y$, $v := -\partial\phi/\partial x$. ϕ represents a vortical motion $\varphi := \phi - y + x$ superimposed on a translation. The vortical motion is simply advected by the velocity field $\vec{v}$ i.e.

$$\frac{D\varphi}{Dt} := \frac{\partial\varphi}{\partial t} + \vec{v}\cdot\nabla\varphi = 0\,,$$

as one can verify by inspection. Thus, variable density exact solutions to the governing equations (4) can be constructed by taking

$$\rho(x,y,t) := f\,(\varphi)$$

with some smooth function f. We used

$$f\,(\varphi) := 2 + (\pi\varphi)^2 \tag{56}$$

The constant on the right hand side is taken to avoid negative densities. The square ensures that densities monotonically increase from the center to the outer boundary of each vortex: a density distribution with local maxima in vortex cores would undergo Rayleigh-Taylor instability. With (56) an exact solution for the density of (4) is

$$\rho(x,y,t) := 2 + 0.5\cos^2(2\pi(x-t))\cos^2(2\pi(y-t)).$$

In table 2 the error norms for the variable density computations are shown. As for the constant density case we obtain second order accuracy both in the 2-norm and in the maximum norm.

TABLE 2

Variable density: errors and convergence rates in the 2-norm and in the maximum norm.

9.2. Advection of a vortex.

We consider the advection of a vortex in a channel. The computational domain is the rectangle $[0,4]\times[0,1]$. The upper and lower boundaries are walls; periodic boundary

conditions are imposed at the left and right boundaries. The grid consists of 80×20 cells. The initial velocity field is:

$$\rho(x,y,0) = 1, \quad p(x,y,0) = 1, \quad u(x,y,0) = 1 - v_\theta(r)\sin\theta, \quad v(x,y,0) = v_\theta(r)\cos\theta$$

with

$$v_\theta(r) = \begin{cases} r/0.2 & \text{if } 0 < r < 0.2 \\ 2 - r/0.2 & \text{if } R < r < 0.4 \\ 0 & \text{if } r > 0.4 \end{cases} \quad \text{and} \quad r = \sqrt{(x-0.5)^2 + (y-0.5)^2}$$

For the above initial data the exact velocity for $t > 0$ can be computed: $u(x,y,t) = u(x - u_\infty t, y, 0)$ and $v(x,y,t) = v(x - u_\infty t, y, 0)$ i.e. the initial data are simply advected by the background velocity u_∞. This problem was originally proposed by *Gresho et al.* [27]. In figure 2 we show contour lines of the stream function for three computations. They have been done using different slope limiters in the MUSCL step of the Godunov type method for the computation of the auxiliary fluxes. Due to the rough discretization

FIG. 2. Advection of a vortex at times $t = 0.0,\ 1.0,\ 2.0,\ 3.0$: 9 contour lines of the stream-function in [0.02,0.18]. Unlimited slopes (top), monotonized central-difference (middle) and Sweby's limiter with $k := 1.8$ (bottom).

the results exhibit a significant deformation of the vortex. In contrast to the results shown in [27] figure 13, however, the core of the vortex is advected along the axis of the channel in agreement with the exact solution. The first computation (unlimited slopes) shows a loss of vorticity comparable with [27] by exhibiting a stronger deformation of the vortex. The second and the third computations (monotonized central-difference and Sweby's limiter with $k := 1.8$, see e.g. *Schulze-Rinne* [36]) show even stronger deformation of the initial vorticity distribution.

9.3. Driven cavity flows.

The driven cavity test problems proposed in [28] have been the subject of many numerical computations, see e.g. [37], [4]. For Reynolds numbers (Re) up to 1000 most computations seem to converge towards a steady state and there is an excellent agreement between stationary solutions obtained with different numerical schemes. Thus, these problems are very well suited to validate new numerical methods. Here driven cavity flows at Reynolds numbers 100 and 1000 have been computed. Our main goals are

- Show that the method can be easily extended to cope with viscous flows.
- Investigate the behavior of the method with respect to the coupling between pressure and velocity fields.
- Investigate the behavior of the method with respect to convergence towards stationary solutions.
- Compare our numerical results with established reference solutions.

In agreement with [28], we consider a viscous zero Mach number flow with no heat conduction. Viscous effects only enter in the momentum equation through a viscous stress and are accounted for as explained in paragraph 3.1.

A delicate issue in the numerical computation of incompressible flows is that of the coupling between pressure and velocity fields. For finite discretizations this problem (often referred to as "local grid decoupling" or "checker-board instability") can be described as follows. Assume that the null space of the discrete gradient operator, $\ker(G_\nu^{\overline{\nu}})$, contains highly oscillating fields. Since $G_\nu^{\overline{\nu}}$ has a local stencil this is usually the case whenever $\dim(\ker(G_\nu^{\overline{\nu}})) > 1$. If the solution $p_{\overline{\nu}}$ of the Poisson-type problem (44) has components in $\ker(G_\nu^{\overline{\nu}})$ one obtains pressure oscillations which do not influence the velocity field: pressure and velocity field decouple.

For two-dimensional equally spaced Cartesian grids and the implementation described in appendix A.3 one finds that $\dim(\ker(G_\nu^{\overline{\nu}})) = 2$ and $\ker(G_\nu^{\overline{\nu}})$ contains, beside constant pressures $p_{\overline{\nu}}^c$, a non-trivial highly oscillating mode $p_{\overline{\nu}}^o$. Therefore, we expect to observe pressure-velocity decoupling whenever the iterative linear system solver for (44) converges towards solutions $p_{\overline{\nu}}$ with components in $\ker(G_\nu^{\overline{\nu}})$. The method of conjugate gradients preserves, by exact arithmetics, the components of $p_{\overline{\nu}}^k$ in $\ker(G_\nu^{\overline{\nu}})$. Since we always start our iteration with $p_{\overline{\nu}}^0 := 0$ we expect a numerical solution obtained in a reasonable number of iteration steps to be oscillation free. This is confirmed by our numerical results. On the other hand numerical solutions obtained through a random choice of $p_{\overline{\nu}}^0$ may exhibit pressure-velocity decoupling.

The understanding of the pressure-velocity decoupling in the limit of vanishing grid size requires a deeper analysis. We have investigated numerically the effects (1) of grid refinement at constant convection-based Courant number C of 0.8 and (2) of time step refinement for a fixed grid size. Some results are shown in figures 3 and 4. Neither in the first nor in the second case do we observe the onset of pressure-velocity decoupling.

FIG. 3. Driven cavity at $Re = 100$, $C = 0.8$: 30 contour lines of the nodal pressure $p_{\overline{\nu}}^{(2)}$ in $[-0.4, 0.4]$. 64×64 (left) and 256×256 (right) grid cells.

FIG. 4. Driven cavity at $Re = 100$, 64×64 grid cells: 30 contour lines of the nodal pressure $p_{\overline{\nu}}^{(2)}$ in $[-0.4, 0.4]$. $C = 0.08$ (left) and $C = 0.008$ (right).

Figure 5 shows the time history of the residual

$$r_2^n := \sum_{\mathcal{V} \in V} h^2 \|\mathbf{U}_{\mathcal{V}}^n - \mathbf{U}_{\mathcal{V}}^{n-1}\|_2$$

for a $Re = 1000$ computation on several grids. The residual is plotted versus the number of computational steps. The cost of a single step on a 64×64 grid is of about 1.3 seconds on a DEC Alpha 21164 CPU running at 500 MHz. For the 128×128 grid cells computation

FIG. 5. Driven cavity at $Re = 1000$: Residual versus number of iterations for 32×32, 64×64 and 128×128 grid cells computations; coarser grid solutions have been taken as initial data for finer grid solutions.

pressure and streamlines of the numerical solution after 5000 time steps are shown in figures 6 and 7. These results are in a good qualitative agreement with the ones presented by *Ghia et al.* [28] page 400. For a more quantitative comparison the horizontal (vertical) component of the velocity along the vertical (horizontal) line through the geometric center

FIG. 6. Driven cavity at $Re = 1000$, 128×128 grid cells: 30 contour lines of the nodal pressure $p_{\mathcal{V}}^{(2)}$ in [-0.4;0.4] (left) and streamlines (right). Streamline values and labels are taken from [28].

FIG. 7. Driven cavity at Re=1000, 128×128 grid cells: streamlines in the left and right bottom secondary vortices. Values and labels are taken from [28].

FIG. 8. Driven cavity at Re=1000, 128×128 grid cells: horizontal (vertical) component of the velocity along the vertical (horizontal) line through the geometric center of the cavity; present results (solid line) and reference solution from [28] (dots).

of the cavity have been drawn in figure 8. The solid line represents the numerical solution obtained with the present method. The dots are values of a reference solution, taken from [28]. The accuracy of this solution has been confirmed by many independent computations.

9.4. Falling droplet.

A heavy "droplet" falls through a light fluid atmosphere and impacts into the surface of the heavy fluid in a cavity. The density ratio is 1000:1 and the Froude number equal to one. The flow is assumed to be inviscid and there is no account for surface tension or for a change of the equation of state (hence, the quotes on "droplet"!). The computational domain is the rectangle $[0, 1] \times [0, 2]$. We present both two- and three-dimensional computations. The goal is to investigate the capability of the method to cope with large density variations. From the numerical point of view the effect of density variations is to increase the condition number of the discrete Poisson-type operators associated to the numerical computation of the pressure $p^{(2)}$. We expect poor convergence in the iterative solution of the linear systems and, in the worst case, oscillations in the pressure field $p_{\mathcal{I}}^{(2)}$. Since our interface pressures $p_{\mathcal{I}}^{(2)}$ are computed via a discrete Poisson-type operator which, for two-dimensional equally spaced Cartesian grids, exhibits local grid decoupling, we are particularly interested in the behavior of $p_{\mathcal{I}}^{(2)}$ in the two dimensional case.

9.4.1. Two-dimensional case.

This problem was originally proposed in *Puckett et al.* [13] to test a tracking method for incompressible variably density flows. Here the interface between light and heavy fluid is captured but we still expect our second order method to properly describe the main features of the flow. The computational grid consists of 64×128 cells. The initial data are:

$$\rho(x, y, 0) = \begin{cases} 1000.0 & \text{if } \ 0.0 \le y \le 1.0 \ \text{ or } \ 0.0 \le r \le 0.2 \\ 1.0 & \text{if } \ 1.0 < y \le 2.0 \ \text{ or } \ 0.2 < r \end{cases}$$

$$p(x, y, 0) = 1, \quad \vec{v}(x, y, 0) = 0 \quad \text{and} \quad r = \sqrt{(x - 0.5)^2 + (y - 1.75)^2}$$

Figure 9 shows density contours at a sequence of output times. After the impact of the droplet some areas of lighter fluid appear within the heavy fluid (last three frames). This is consistent with the results shown in [13] where this effect was referred to as "trapped air bubbles". Figure 10 shows contour lines of the cell interface pressure $p_{\mathcal{I}}^{(2)}$ as the droplet hits the surface of the heavy fluid in the cavity. We do not notice spurious oscillations or local

FIG. 9. Two-dimensional falling "droplet" at $Fr = 1$ and density ratio 1000: Contour lines of density in [1,1000].

FIG. 10. Two-dimensional falling "droplet" at $Fr = 1$ and density ratio 1000: 10 contour lines of the cell interface pressure $p_{\mathcal{I}}^{(2)}$ at -999, -990, -900, -800, -600, -400, -200, 0, 200 and 400 (left) and 10 contour lines of the density in [1,1000] (right) at $t = 1.125$.

grid decoupling effects. The multi-grid preconditioned conjugate gradients technique allows the iterative solution of the linear systems for the pressure in about the same number of iterations as for the constant density case.

9.4.2. Three-dimensional case.

This is a simple extension of the previous case to three space dimensions. The grid consists of $64 \times 64 \times 128$ cells. The initial data are:

$$\rho(x,y,0) = \begin{cases} 1000.0 & \text{if } 0.0 \le z \le 1.0 \text{ or } 0.0 \le r \le 0.2 \\ 1.0 & \text{if } 1.0 < z \le 2.0 \text{ or } 0.2 < r \end{cases}$$

$$p(x,y,0) = 1, \quad \vec{v}(x,y,0) = 0 \quad \text{and} \quad r = \sqrt{(x-0.5)^2 + (y-0.5)^2 + (z-1.75)^2}$$

Figure 11 shows the density iso-surface 500 as the droplet falls and impacts into the surface of the heavy fluid in the closed cavity.

FIG. 11. Three-dimensional falling "droplet" at $Fr = 1$ and density ratio 1000: Iso-surface $\rho = 500$ of density.

9.5. Thermo-acoustic refrigerator.

This example shows that our method can treat compressible zero Mach number flows with heat conduction. A thermo-acoustic refrigerator basically consists of a resonance tube, a stack of plates, two heat exchangers and an acoustic driver (usually a loudspeaker). The basic components of a thermo-acoustic refrigerator are sketched below : The flow within

FIG. 12. Sketch of a simplified thermo-acoustic refrigerator.

the tube is characterized by two length scales, namely the short hydrodynamic and the long acoustic scale. The Mach number in the tube is very small, typically $\mathcal{O}(10^{-3})$. Thus, the flow between the plates, which are much shorter than the tube, can be assumed to be incompressible with a prescribed velocity field imposed on the inlet and outlet boundaries. The calculation focuses on the flow along the plate and the heat exchangers. The plate is modeled as a zero thickness plate with finite thermal mass. The thickness of the heat exchangers is zero as well. The geometry of the domain is shown below. The problem is defined in terms of several characteristic numbers: the Prandtl number Pr, the Reynolds number Re and the ratio of specific heats γ. The temperatures of the heat exchangers T_{hot},

FIG. 13. Computational domain (dotted line).

T_{cold} are kept constant. The temperature distribution within the plate is governed by a heat conduction equation:

$$\frac{\partial T}{\partial t} = \frac{1}{Pe_s}\left(\frac{\partial^2}{\partial x^2}T + \frac{2\kappa}{\lambda}\frac{\partial}{\partial y}T\Big|_{\mathrm{gas}}\right) \tag{57}$$

Where Pe_s denotes the Peclet number of the solid, κ represents the ratio of the thermal conductivities, λ is the thermal penetration depth. The specific values are listed below. After 200 acoustic cycles a periodical solution is reached. Figure (14) shows the temperature

TABLE 3
Specific numbers.

at different times during the 201-th acoustic cycle. The heat fluxes through the surface of the exchangers during an acoustic cycle are shown in figure (15).

FIG. 14. Temperature field during different times of an acoustic cycle; $T := 2\pi$.

FIG. 15. Heat fluxes through the surface of the hot (left) and cold (right) heat exchanger during an acoustic cycle.

10. CONCLUSIONS AND FUTURE WORK

Summary and Conclusions. This paper demonstrates that a finite volume compressible flow solver can be extended to handle incompressible, zero Mach number flows. Our approach is general enough to include a wide variety of underlying compressible flow schemes. The major ingredients of the required extensions are two pressure Poisson-solutions. These allow us to enforce zero Mach number elliptic divergence constraints for the convective numerical fluxes as well as for the final cell centered velocity fields.

The design of the scheme directly draws on a low Mach number asymptotic analysis of the governing equations in conservation form. The analysis, which was presented in [19], shows how the well-known velocity divergence constraint of incompressible flows emerges in a natural way from an associated divergence constraint on the energy flux as the Mach number vanishes. The insight gained in this way is used to construct numerical fluxes of mass, momentum and energy that are consistent with the zero Mach number limit. The scheme thus represents a discretization of the full conservation equations rather than one of an asymptotic limit system which would explicitly introduce a velocity divergence constraint!

The computational examples given are chosen to demonstrate various features of the proposed method. Thus we show second order accuracy for a test problem proposed by Almgren et al., [33], and we obtain competitive results on the test problem of an advected zero circulation vortex as proposed by Gresho and Chen, [27]. After adding a first order in time extension to viscous incompressible flow, we find very close agreement with published

results in the literature for standard driven cavity test problems (see Ghia, Ghia & Shin, [28]). Notably, grid refinement at constant convection-based CFL number of 0.8 as well as decreasing time steps at constant spacial resolution do not affect the results. This suggests stability and convergence of the method, even though we cannot provide rigorous proofs at this stage. Excellent behavior of the scheme is found for variable density flows. A "falling droplet" with a density ratio of 1000, simulated by a suitable choice of an initial entropy distribution in an ideal gas, is handled without evidence of pressure, velocity or density oscillations.

Current limitations and future work. The asymptotics in [19] has been carried out for an ideal gas equation of state assuming constant ratio of heat capacities. A consequence is that the total energy per unit volume, which is the conserved energy quantity in our numerical scheme, is proportional to pressure to leading and first order in the Mach number. This simplifies the formulation of the asymptotic limiting form of the energy equation and, hence, the set-up of the numerical method.

In the present paper we have restricted ourselves to the zero Mach number limit, but considered multi-dimensional flows. In contrast, [19] was restricted to one space dimension for the numerics, but allowed small, but non-zero Mach numbers. The obvious next step is to combine the approaches and construct a method that allows a smooth transition from fully compressible to zero Mach number. A first realization of this generalization of the present ideas has been described by one of the authors in [18].

The original motivation for this work stems from combustion applications; notably from the desire to simulate deflagration-to-detonation transitions, where, throughout a computation, the Mach number would vary from $M \approx 10^{-4}$ to $M \approx 10$. Thus, two of our further goals are (i) to extend the scheme to include chemical reactions for resolved computations of combustion processes at arbitrary Mach number and (ii) to combine the present technology with the flame front capturing-tracking ideas from [40] (compressible flow) and [29] (zero Mach number combustion).

ACKNOWLEDGMENT

We thank the Deutsche Forschungsgemeinschaft for its continuous support of our work. We thank the reviewers for their constructive criticism and their suggestions.

APPENDIX

A.1. FAKE ACOUSTICS IN THE SYSTEM I^* REMAIN SMALL

Let $\vec{v}(\vec{x},t)$, $p(\vec{x},t)$ be a smooth solution of the auxiliary system (9) for initial data $\vec{v}(\vec{x},0)$, $p(\vec{x},0)$ such that

$$\nabla \cdot \vec{v}(\vec{x},0) = 0$$
$$\nabla p(\vec{x},0) = \nabla p^{(0)}(\vec{x},0) = 0\,.$$

From (9.3), (9.4) one has

$$\begin{aligned} p_t(\vec{x},0) &= (\gamma-1)(\rho e)_t(\vec{x},0) \\ &= -(\gamma-1)\nabla\cdot\left((\rho e(\vec{x},0)+p(\vec{x},0))\,\vec{v}(\vec{x},0)\right) \\ &= -\nabla\cdot\left(\gamma\,p(\vec{x},0)\,\vec{v}(\vec{x},0)\right) \\ &= -\gamma\,\vec{v}(\vec{x},0)\cdot\nabla p(\vec{x},0) - \gamma\,p(\vec{x},0)\,\nabla\cdot\vec{v}(\vec{x},0) \\ &= \quad 0\,. \end{aligned}$$

Expanding $\vec{v}(\vec{x},t)$ and $p(\vec{x},t)$ about $t=0$ and using the above equations yields

$$\begin{aligned} \nabla\cdot\vec{v}(\vec{x},t) &= \nabla\cdot\vec{v}(\vec{x},0) + \mathcal{O}(t) = \mathcal{O}(t) \\ \nabla p(\vec{x},t) &= \nabla p(\vec{x},0) + \nabla p_t(\vec{x},0)t + \mathcal{O}(t^2) = \mathcal{O}(t^2) \end{aligned}$$

as stated in (11).

A.2. FIRST PROJECTION: DISCRETE POISSON EQUATION

We write the discrete gradient $G_{\mathcal{I}}^{\mathcal{V}}$ and divergence $D_{\mathcal{V}}^{\mathcal{I}}$ for a two dimensional Cartesian grid of constant spacings δx and δy and derive the explicit form of the Poisson-like equation (32).The double index (i,j) is used to tag a cell value. The indexes $(i+1/2,j)$, $(i,j+1/2)$ are used for interface values between the cells (i,j), $(i+1,j)$ and (i,j), $(i,j+1)$ respectively. The discrete gradient $G_{\mathcal{I}}^{\mathcal{V}}$ is defined as follows

$$\begin{aligned} G^{\mathcal{V}}_{i+1/2,j}\left(p_{\mathcal{V}}\right) &:= \begin{pmatrix} \dfrac{p_{i+1,j}-p_{i,j}}{\delta x} \\ \dfrac{p_{i,j+1}-p_{i,j-1}+p_{i+1,j+1}-p_{i+1,j-1}}{4\delta y} \end{pmatrix} \\ G^{\mathcal{V}}_{i,j+1/2}\left(p_{\mathcal{V}}\right) &:= \begin{pmatrix} \dfrac{p_{i+1,j}-p_{i-1,j}+p_{i+1,j+1}-p_{i-1,j+1}}{4\delta x} \\ \dfrac{p_{i,j+1}-p_{i,j}}{\delta y} \end{pmatrix}. \end{aligned}$$

The discrete divergence $D_{\mathcal{V}}^{\mathcal{I}}$ is, according to equation (31)

$$D^{\mathcal{I}}_{i,j}\left(\vec{v}_{\mathcal{I}}\right) := \frac{u_{i+1/2,j}-u_{i-1/2,j}}{\delta x} + \frac{v_{i,j+1/2}-v_{i,j-1/2}}{\delta y}$$

with $\vec{v}_{\mathcal{I}} := (u_{\mathcal{I}}, v_{\mathcal{I}})$. With these definitions $D_{\mathcal{V}}^{\mathcal{I}} G_{\mathcal{I}}^{\mathcal{V}}$ is the standard 5-points Laplacian

$$D^{\mathcal{I}}_{i,j}\left(G^{\mathcal{V}}_{\mathcal{I}}\left(p_{\mathcal{V}}\right)\right) := \frac{p_{i+1,j}-2p_{i,j}+p_{i-1,j}}{\delta x^2} + \frac{p_{i,j+1}-2p_{i,j}+p_{i,j-1}}{\delta y^2}.$$

and the (i,j)-th equation of the linear system (32) for the cell values $p_{\mathcal{V}}$ reads

$$\begin{aligned} &\frac{h^{0,*}_{i+1/2,j}p^{(2)}_{i+1,j} - \left(h^{0,*}_{i+1/2,j}+h^{0,*}_{i-1/2,j}\right)p^{(2)}_{i,j} + h^{0,*}_{i-1/2,j}p^{(2)}_{i-1,j}}{\delta x^2} + \\ &\frac{h^{0,*}_{i,j+1/2}p^{(2)}_{i,j+1} - \left(h^{0,*}_{i,j+1/2}+h^{0,*}_{i,j-1/2}\right)p^{(2)}_{i,j} + h^{0,*}_{i,j-1/2}p^{(2)}_{i,j-1}}{\delta y^2} = \\ &\frac{2}{\delta t}\left(\frac{F^{*}_{\rho e;i+1/2,j}-F^{*}_{\rho e;i-1/2,j}}{\delta x} + \frac{G^{*}_{\rho e;i,j+1/2}-G^{*}_{\rho e;i,j-1/2}}{\delta y}\right) + \frac{2}{\delta t}\frac{1}{\gamma-1}\frac{dp^{(0)}}{dt}. \end{aligned}$$

with $F^*_{\rho e;i+1/2,j} := (\rho h^0 u)^*_{i+1/2,j}$ and $G^*_{\rho e;i,j+1/2} := (\rho h^0 v)^*_{i,j+1/2}$.

A.3. SECOND PROJECTION: DISCRETE POISSON EQUATION

We write the discrete gradient $G^{\overline{\nu}}_{\nu}$ and the divergence $D^{\nu}_{\overline{\nu}}$ for a two dimensional regular Cartesian grid and derive the explicit form of the Poisson-like equation (44). Beside the notation introduced in the previous section we use the double index $(i+1/2, j+1/2)$ to tag node values. The indexes $(i+1, j+1/2)$, $(i+1/2, j+1)$ are used for interface values between the node centered control volumes $(i+1/2, j+1/2)$, $(i+3/2, j+1/2)$ and $(i+1/2, j+1/2)$, $(i+1/2, j+3/2)$ respectively (figure 1). The linear operators $L^{\overline{\nu}}_{\mathcal{I}}(p_{\overline{\nu}})$,

FIG. 1. Two dimensional Cartesian grid.

$L^{\nu}_{\mathcal{I}}(\vec{v}_{\nu})$ are defined as follows

$$\begin{aligned}
L^{\overline{\nu}}_{i+1/2,j}\left(p_{\overline{\nu}}\right) &:= \frac{1}{2}\left(p_{i+1/2,j+1/2} + p_{i+1/2,j-1/2}\right)\\
L^{\overline{\nu}}_{i,j+1/2}\left(p_{\overline{\nu}}\right) &:= \frac{1}{2}\left(p_{i-1/2,j+1/2} + p_{i+1/2,j+1/2}\right)\\
L^{\nu}_{i+1,j+1/2}\left(\vec{v}_{\nu}\right) &:= \frac{1}{2}\left(\vec{v}_{i+1,j+1} + \vec{v}_{i+1,j}\right)\\
L^{\nu}_{i+1/2,j+1}\left(\vec{v}_{\nu}\right) &:= \frac{1}{2}\left(\vec{v}_{i,j+1} + \vec{v}_{i+1,j+1}\right)
\end{aligned}$$

With these definitions the discrete gradient $G^{\overline{\nu}}_{\nu}$ is, according to equation (37)

$$\begin{aligned}
G^{\overline{\nu}}_{i,j}\left(p_{\overline{\nu}}\right) &= \begin{pmatrix} \dfrac{L^{\overline{\nu}}_{i+1/2,j}(p_{\overline{\nu}}) - L^{\overline{\nu}}_{i-1/2,j}(p_{\overline{\nu}})}{\delta x} \\ \dfrac{L^{\overline{\nu}}_{i,j+1/2}(p_{\overline{\nu}}) - L^{\overline{\nu}}_{i,j-1/2}(p_{\overline{\nu}})}{\delta y} \end{pmatrix}\\
&= \begin{pmatrix} \dfrac{p_{i+1/2,j+1/2} - p_{i-1/2,j+1/2} + p_{i+1/2,j-1/2} - p_{i-1/2,j-1/2}}{2\delta x} \\ \dfrac{p_{i+1/2,j+1/2} - p_{i+1/2,j-1/2} + p_{i-1/2,j+1/2} - p_{i-1/2,j-1/2}}{2\delta y} \end{pmatrix}.
\end{aligned}$$

After (42) the divergence $D^{\nu}_{\overline{\nu}}$ is

$$\begin{aligned}
D^{\nu}_{i+1/2,j+1/2}\left(\vec{v}_{\nu}\right) &= \frac{L^{\nu}_{i+1,j+1/2}\left(u_{\nu}\right) - L^{\nu}_{i,j+1/2}\left(u_{\nu}\right)}{\delta x} + \\
&\quad \frac{L^{\nu}_{i+1/2,j+1}\left(v_{\nu}\right) - L^{\nu}_{i+1/2,j}\left(v_{\nu}\right)}{\delta y}\\
&= \frac{u_{i+1,j+1} - u_{i,j+1} + u_{i+1,j} - u_{i,j}}{2\delta x} + \\
&\quad \frac{v_{i,j+1} - v_{i,j} + v_{i+1,j+1} - v_{i+1,j}}{2\delta y}.
\end{aligned}$$

With the above definitions $D^{\nu}_{\overline{\nu}}(G^{\overline{\nu}}_{\nu}(p_{\overline{\nu}}))$ is the standard 9-points Laplacian

$$D^{\nu}_{i+1/2,j+1/2}\left(G^{\overline{\nu}}_{\nu}\left(p_{\overline{\nu}}\right)\right) = \frac{1}{4}\frac{\delta x^2 + \delta y^2}{\delta x^2 \delta y^2} a_{i+1/2,j+1/2} - \frac{1}{2}\frac{\delta x^2 - \delta y^2}{\delta x^2 \delta y^2} b_{i+1/2,j+1/2}$$

with

$$
\begin{aligned}
a_{i+1/2,j+1/2} &:= p_{i+3/2,j+3/2} + p_{i-1/2,j+3/2} + p_{i-1/2,j-1/2} + p_{i+3/2,j-1/2} - 4p_{i+1/2,j+1/2} \\
b_{i+1/2,j+1/2} &:= p_{i+3/2,j+1/2} - p_{i+1/2,j+3/2} + p_{i-1/2,j+1/2} - p_{i+1/2,j-1/2}.
\end{aligned}
$$

For $\delta x = \delta y$ the second term on the right hand side of the discrete Laplacian disappears and the stencil of $D_{\overline{\nu}}^{\nu}(G_{\nu}^{\overline{\nu}}(p_{\overline{\nu}}))$ reduces to a five diagonal point stencil. The $(i+1/2, j+1/2)$-th equation of the linear system (44) becomes

$$
\begin{aligned}
&\frac{1}{4\delta x^2}\Big[\; h_{i+1,j+1}^{n+1}\left(p_{i+3/2,j+3/2}^{(2)} - p_{i+1/2,j+3/2}^{(2)} + p_{i+3/2,j+1/2}^{(2)} - p_{i+1/2,j+1/2}^{(2)}\right) - \\
&\qquad h_{i,j+1}^{n+1}\left(p_{i+1/2,j+3/2}^{(2)} - p_{i-1/2,j+3/2}^{(2)} + p_{i+1/2,j+1/2}^{(2)} - p_{i-1/2,j+1/2}^{(2)}\right) + \\
&\qquad h_{i+1,j}^{n+1}\left(p_{i+3/2,j+1/2}^{(2)} - p_{i+1/2,j+1/2}^{(2)} + p_{i+3/2,j-1/2}^{(2)} - p_{i+1/2,j-1/2}^{(2)}\right) - \\
&\qquad h_{i,j}^{n+1}\left(p_{i+1/2,j+1/2}^{(2)} - p_{i-1/2,j+1/2}^{(2)} + p_{i+1/2,j-1/2}^{(2)} - p_{i-1/2,j-1/2}^{(2)}\right)\;\Big] + \\
&\frac{1}{4\delta y^2}\Big[\; h_{i,j+1}^{n+1}\left(p_{i+1/2,j+3/2}^{(2)} - p_{i+1/2,j+1/2}^{(2)} + p_{i-1/2,j+3/2}^{(2)} - p_{i-1/2,j+1/2}^{(2)}\right) - \\
&\qquad h_{i,j}^{n+1}\left(p_{i+1/2,j+1/2}^{(2)} - p_{i+1/2,j-1/2}^{(2)} + p_{i-1/2,j+1/2}^{(2)} - p_{i-1/2,j-1/2}^{(2)}\right) + \\
&\qquad h_{i+1,j+1}^{n+1}\left(p_{i+3/2,j+3/2}^{(2)} - p_{i+3/2,j+1/2}^{(2)} + p_{i+1/2,j+3/2}^{(2)} - p_{i+1/2,j+1/2}^{(2)}\right) - \\
&\qquad h_{i+1,j}^{n+1}\left(p_{i+3/2,j+1/2}^{(2)} - p_{i+3/2,j-1/2}^{(2)} + p_{i+1/2,j+1/2}^{(2)} - p_{i+1/2,j-1/2}^{(2)}\right)\;\Big] \\
&= \\
&\frac{1}{\delta t}\frac{1}{2\delta x}\Big[\; h_{i+1,j+1}^{n+1}\rho u_{i+1,j+1}^{**} - h_{i,j+1}^{n+1}\rho u_{i,j+1}^{**} + h_{i+1,j}^{n+1}\rho u_{i+1,j}^{**} - h_{i,j}^{n+1}\rho u_{i,j}^{**}\;\Big] + \\
&\frac{1}{\delta t}\frac{1}{2\delta y}\Big[\; h_{i,j+1}^{n+1}\rho v_{i,j+1}^{**} - h_{i,j}^{n+1}\rho v_{i,j}^{**} + h_{i+1,j+1}^{n+1}\rho v_{i+1,j+1}^{**} - h_{i+1,j}^{n+1}\rho v_{i+1,j}^{**}\;\Big].
\end{aligned}
$$

REFERENCES

1. Pember R. B., Howell L. H., Bell J. B., Colella P., Crutchfield W. Y., Fiveland W. A., and Jessee J. P. An adaptive projection method for unsteady, low-mach number combustion. Technical Report LBNL-41339, Ernest Orlando Lawrence Berkeley National Laboratory, 1998.
2. J. Bell, P. Colella, and H. Glaz. A second-order projection method for the incompressible Navier-Stokes equations. UCRL Preprint 98225, 1988.
3. J. Bell and D. Marcus. A Second-Order Projection Method for Variable-Density Flows. *J. Comput. Phys.*, 101:334–348, 1992.
4. C. H. Bruneau and C. Jouron. An Efficient Scheme for Solving Steady Incompressible Navier-Stokes Equations. *Journal of Computational Physics*, 89:389–413, 1990.
5. Karki K. C. and Patankar S. V. Pressure based calculation procedure for viscous flows at all speeds in arbitrary configurations. *AIAA Journal*, 27:1167–1174, 1989.
6. Viozat C. Implicit upwind schemes for low mach number compressible flows. Technical Report 3084, INRIA, 1997.
7. Zienkiewicz O. C., Szmelter J., and Peraire J. Compressible and incompressible flow: An algorithm for all seasons. *J. Comput. Methods Appl. Mech. Eng.*, 78(1):105–121, 1990.
8. Munz C.-D., Roller S., Klein R., and Geratz K. J. The extension of incompressible flow solvers to the weakly compressible regime. submitted to Theoretic. and Comput. Fluid Modeling, 1997.
9. A. J. Chorin. Numerical Solution of Incompressible Flow Problems. *Studies in Num. Anal.*, 2:64–71, 1968.
10. A. J. Chorin. Numerical Solution of the Navier-Stokes Equations. *Math. Comp.*, 22:745–762, 1968.
11. Turkel E. Preconditioned methods for solving the incompressible and low speed compressible equations. *J. Comput. Phys.*, 72:277–298, 1987.

12. B. Einfeldt. On Godunov type methods for gas dynamics. Inst. f. Geometrie u. Praktische Mathematik, RWTH Aachen, Bericht Nr. 41, 1986.

13. Puckett E. G., Almgren A. S, Bell J. B., Marcus D. L., and Rider W. J. A high-order projection method for tracking fluid interfaces in variable density incompressible flows. *J. Comput. Phys.*, 130:269–282, 1997.

14. Bijl H. and Wesseling P. A unified method for computing incompressible and compressible flows in boundary-fitted coordinates. *J. Comput. Phys.*, 141:153–173, 1998.

15. Guillard H. and Viozat C. On the behavior of upwind schemes in the low mach number limit. Technical Report 3160, INRIA, 1997.

16. Harlow F. H. and Welch J. E. Numerical calculation of time-dependent viscous incompressible flow of fluid with a free surface. *The Physics of Fluids*, 8:2182–2189, 1965.

17. Demirdzic I. and Peric M. Finite volume method for prediction of fluid flow in arbitrarily shaped domains with moving boundaries. *Int. J. Numer. Methods Fluids*, 10(7):771–790, 1990.

18. Geratz K. J. *Erweiterung eines Godunov-Typ-Verfahrens für zwei-dimensionale kompressible Strömungen auf die Fälle kleiner und verschwindender Machzahl*. PhD thesis, Rheinisch-Westfälischen Technischen Hochschule Aachen, D 82, 1997.

19. R. Klein. Semi-implicit extension of a godunov-type scheme based on low mach number asymptotics i: One-dimensional flow. *Journ. of Comp. Physics*, 121:213–237, 1995.

20. Sesterhenn J. L. *Zur numerischen Berechnung kompressibler Strömungen bei kleinen Mach-Zahlen*. PhD thesis, Swiss Federal Institute of Technology, Diss. ETH No. 11334, 1995.

21. Sesterhenn J. L., Müller B., and Thomann H. Flux-vector splitting for compressible low mach number flow. *J. Comput. Fluids*, 22:441–451, 1993.

22. B. van Leer. Towards the ultimate conservative difference scheme. I. The quest of monotonicity. *Lecture Notes in Phys.*, 18:163–168, 1973.

23. B. van Leer. Towards the ultimate conservative difference scheme. II. Monotonicity and conservation combined in a second-order scheme. *J. Comput. Phys.*, 14:361–370, 1974.

24. B. van Leer. Towards the ultimate conservative difference scheme. III. Upstream-centered finite-difference schemes for ideal compressible flow. *J. Comput. Phys.*, 23:263–275, 1977.

25. B. van Leer. Towards the ultimate conservative difference scheme. IV. A new approach to numerical convection. *J. Comput. Phys.*, 23:276–299, 1977.

26. B. van Leer. Towards the ultimate conservative difference scheme. V. A second-order sequel to Godunov's method. *J. Comp. Phys.*, 32:101–136, 1979.

27. Gresho P. M. and Chan S. T. On the Theory of Semi-Implicit Prpjection Methods for Viscous Incompressible Flow and its Implementation via a Finite Element Method that also introduces a Nearly Consistent Mass Matrix. Part 2: Implementation. *Int. J. for Num. Meth. in Fluids*, 11:621–659, 1990.

28. Ghia K. N., Ghia U., and Shin C. T. High-re Solutions for Incompressible Flow using the Navier-Stokes Equations and a multigrid method. *Journal of Computational Physics*, 48:387–411, 1982.

29. Terhoeven P. *Ein numerisches Verfahren zur Berechnung von Flammenfronten bei kleiner Machzahl*. PhD thesis, Rheinisch-Westfälischen Technischen Hochschule Aachen, 22 Mai, 1998.

30. Wesseling P. *An Introduction to multigrid methods*. John Wiley & Sons, Chichester, 1991.

31. Courant R., Friedrichs K. O., and Lewy H. Über die partiellen Differenzengleichungen der Physik. *Math. Ann.*, 100:32, 1928.

32. Sauer R. *Theoretische Einfuehrung in die Gasdynamik*. Springer Verlag, Berlin, 1943.

33. Almgren A. S, Bell J. B., Colella P., Howell L. H., and Welcome M. L. A conservative adaptive projection method for the variable density incompressible navier-stokes equations. Technical Report LBNL-39075, Ernest Orlando Lawrence Berkeley National Laboratory, 1996.

34. Klainerman S. and Majda A. J. Compressible and incompressible fluids. *Commun. Pure Appl. Math.*, 35:629, 1982.

35. Schochet S. Asymptotics for symmetric hyperbolic systems with a large parameter. *J. Diff. Eqs.*, 75:1–27, 1988.

36. C.W. Schulz-Rinne. *The Riemann problem for two-dimensional gas dynamics and new limiters for high-order schemes*. PhD thesis, Swiss Federal Institute of Technology, Diss. ETH No. 10297, 1993.

37. W. Y. Soh and J. W. Goodrich. Unsteady Solution of the Incompressible Navier-Stokes Equations. *Journal of Computational Physics*, 79:113–134, 1988.

38. G. Strang. On the construction and comparison of difference schemes. *SIAM J. Numer. Anal.*, 5:506–517, 1968.

39. Patankar S. V. and Spalding D. B. A calculation procedure for heat, mass, and momentum transfer in three-dimensional parabolic flow. *Int. J. Heat Mass Transfer*, 15:1787–1806, 1972.

40. Smiljanovski V., Moser V., and Klein R. A Capturing-Tracking Hybrid Scheme for Deflagration Discontinuities. *J. Combustion Theory and Modeling*, 1:183–215, 1997.

1. FIGURES

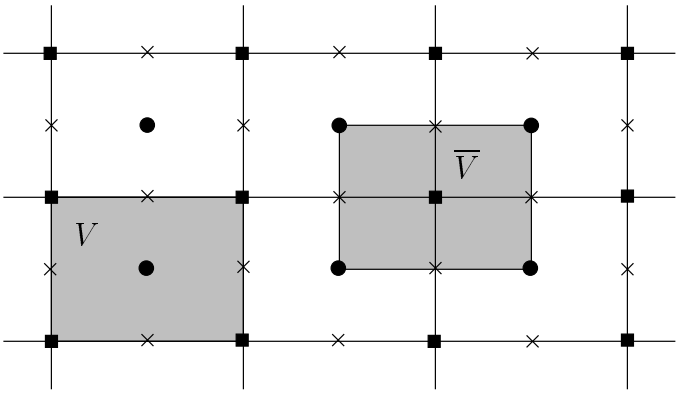

FIG. 1. Cell (V) and node centered ($\overline{V}$) control volumes; cell centers, nodes and the midpoints of the interfaces are marked by circles, squares and crosses, respectively.

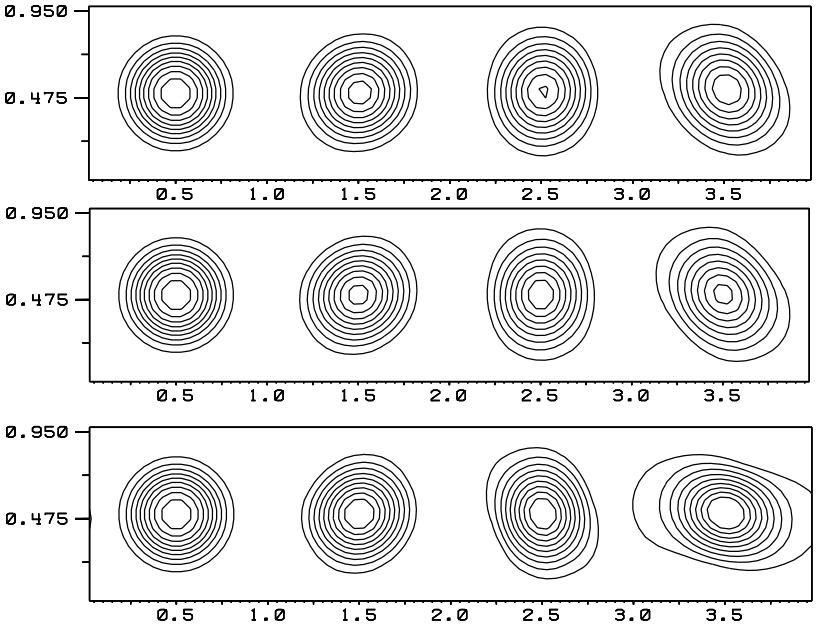

FIG. 2. Advection of a vortex at times $t = 0.0,\ 1.0,\ 2.0,\ 3.0$: 9 contour lines of the stream-function in [0.02,0.18]. Unlimited slopes (top), monotonized central-difference (middle) and Sweby's limiter with $k := 1.8$ (bottom).

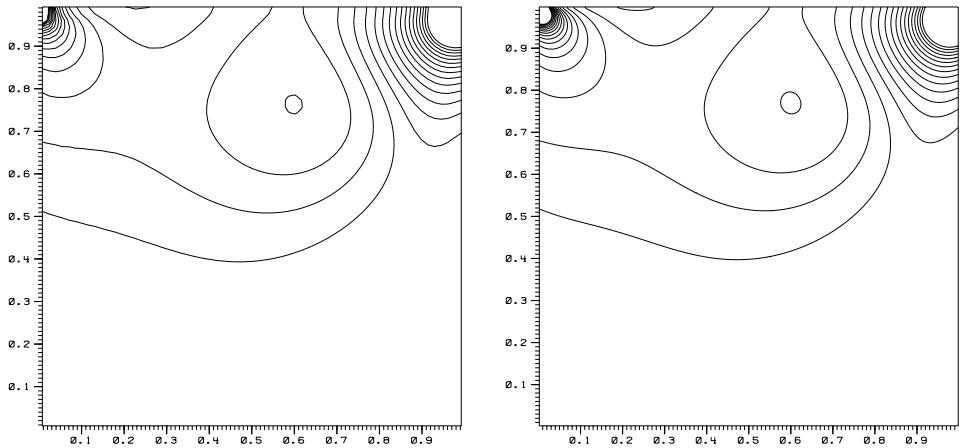

FIG. 3. Driven cavity at $Re = 100$, $C = 0.8$: 30 contour lines of the nodal pressure $p_{\overline{\mathcal{V}}}^{(2)}$ in $[-0.4, 0.4]$. 64×64 (left) and 256×256 (right) grid cells.

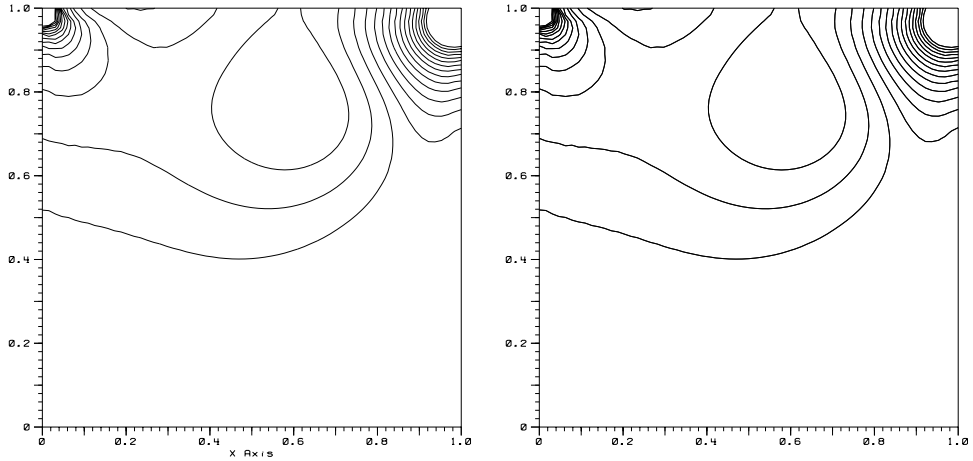

FIG. 4. Driven cavity at $Re = 100$, 64×64 grid cells: 30 contour lines of the nodal pressure $p^{(2)}_{\nu}$ in $[-0.4, 0.4]$. $C = 0.08$ (left) and $C = 0.008$ (right).

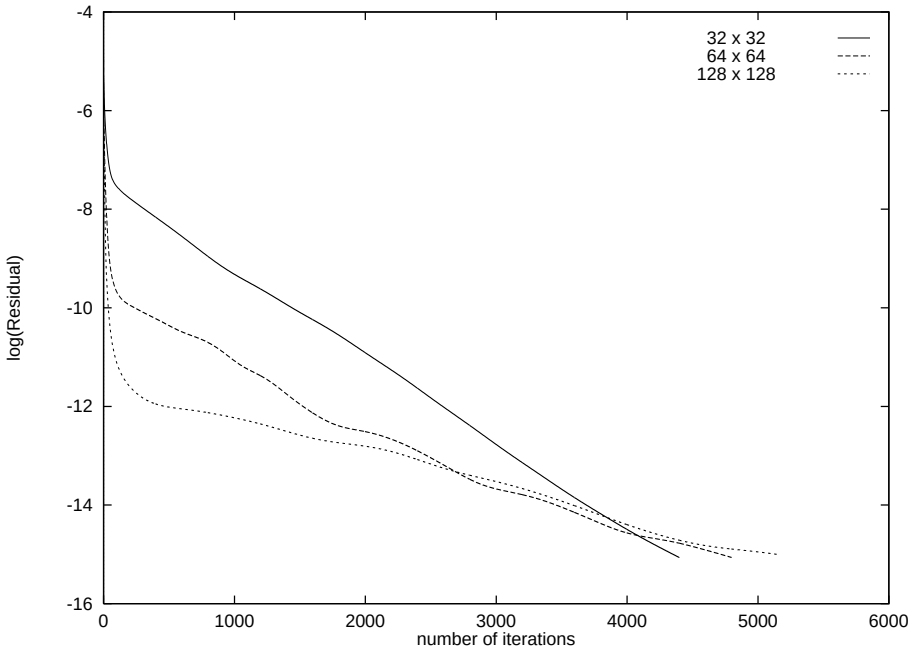

FIG. 5. Driven cavity at $Re = 1000$: Residual versus number of iterations for 32×32, 64×64 and 128×128 grid cells computations; coarser grid solutions have been taken as initial data for finer grid solutions.

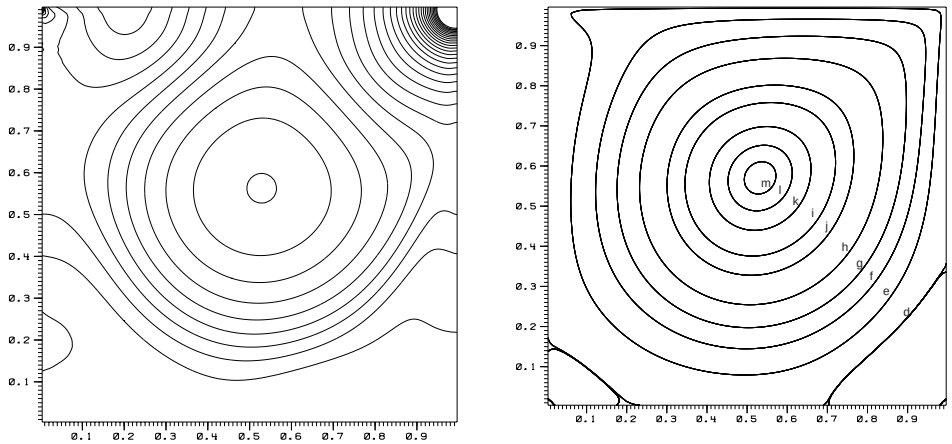

FIG. 6. Driven cavity at $Re = 1000$, 128×128 grid cells: 30 contour lines of the nodal pressure $p_{\mathcal{V}}^{(2)}$ in [-0.4;0.4] (left) and streamlines (right). Streamline values and labels are taken from [28].

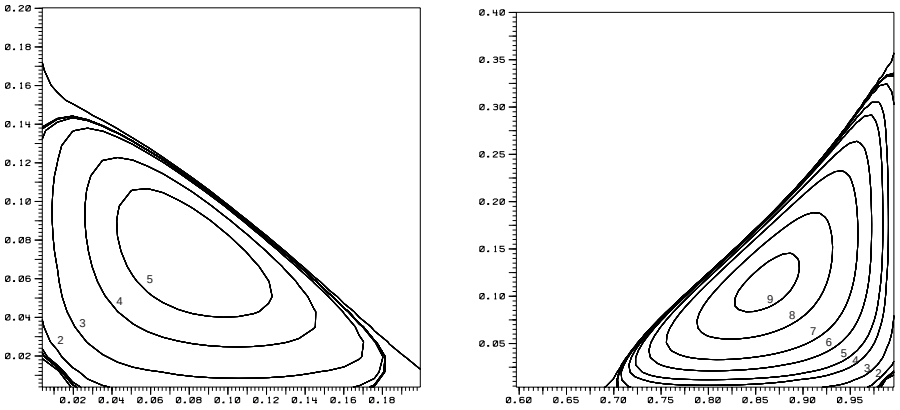

FIG. 7. Driven cavity at Re=1000, 128×128 grid cells: streamlines in the left and right bottom secondary vortices. Values and labels are taken from [28].

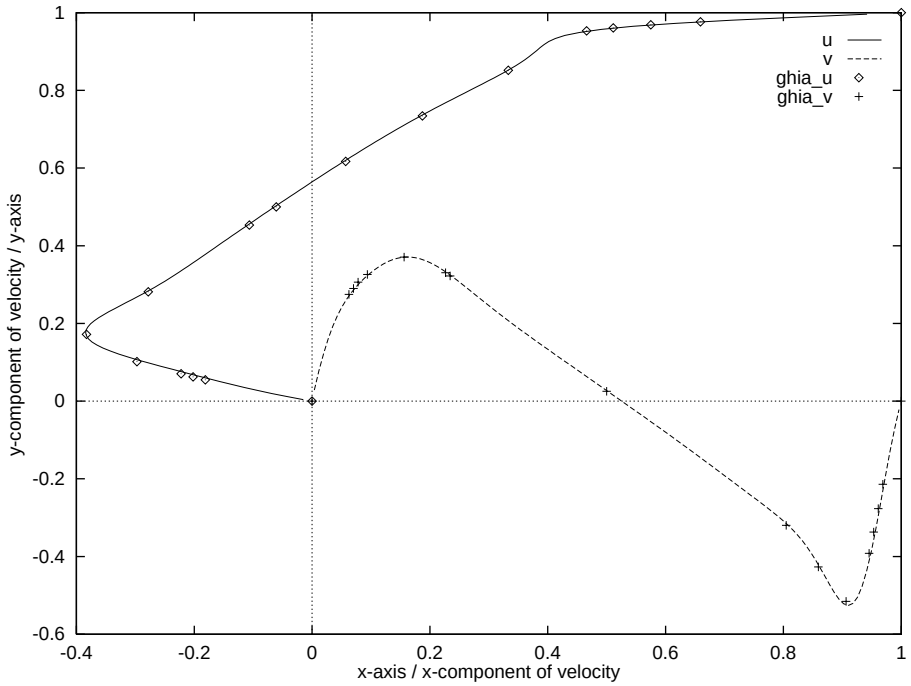

FIG. 8. Driven cavity at Re=1000, 128×128 grid cells: horizontal (vertical) component of the velocity along the vertical (horizontal) line through the geometric center of the cavity; present results (solid line) and reference solution from [28] (dots).

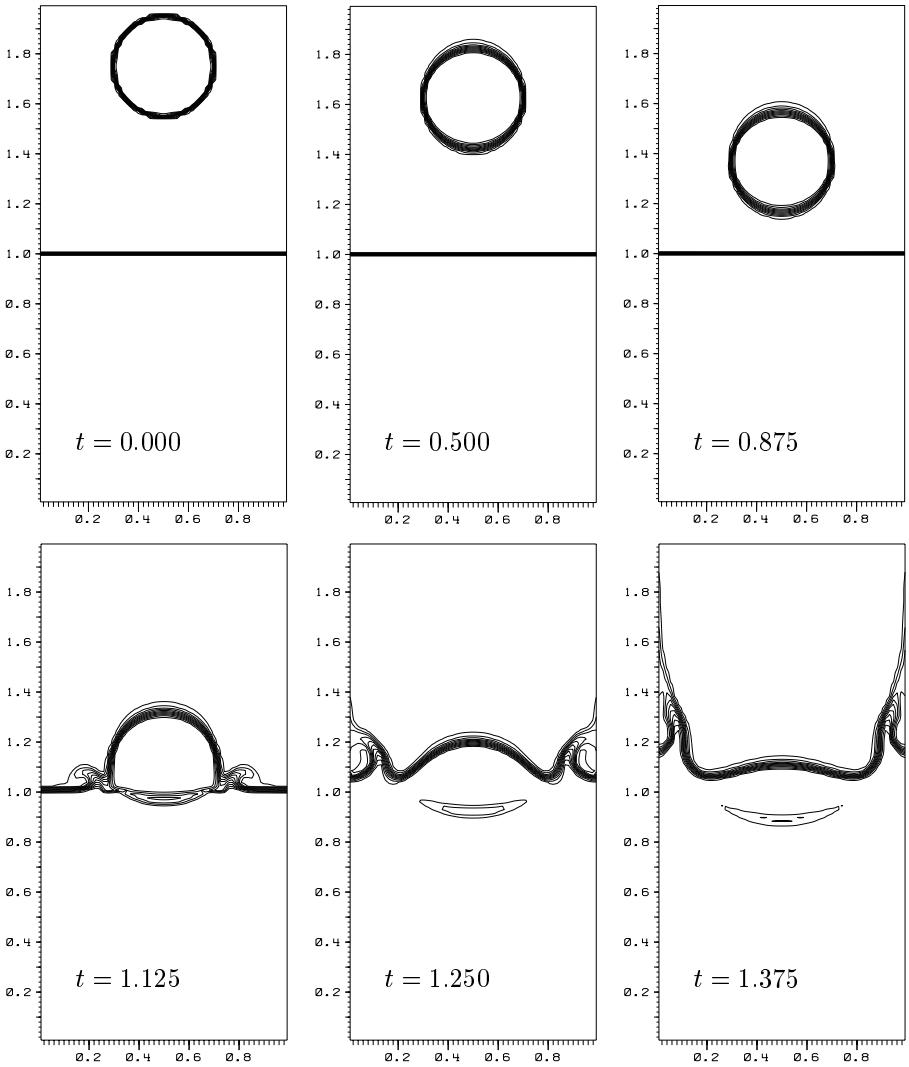

FIG. 9. Two-dimensional falling "droplet" at $Fr = 1$ and density ratio 1000: Contour lines of density in [1,1000].

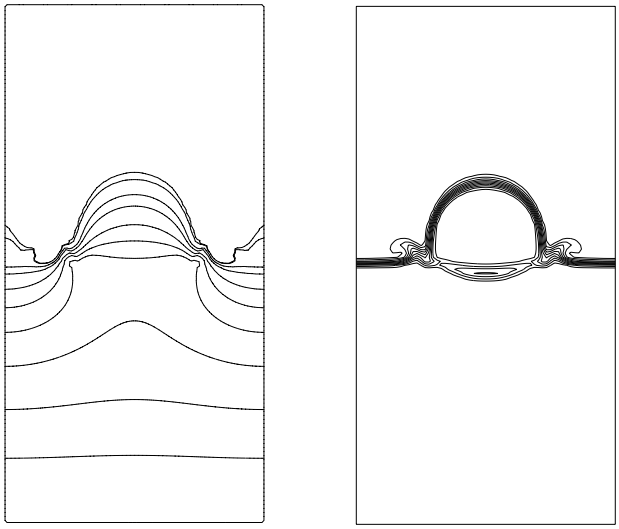

FIG. 10. Two-dimensional falling "droplet" at $Fr = 1$ and density ratio 1000: 10 contour lines of the cell interface pressure $p_{\mathcal{I}}^{(2)}$ at -999, -990, -900, -800, -600, -400, -200, 0, 200 and 400 (left) and 10 contour lines of the density in [1,1000] (right) at $t = 1.125$.

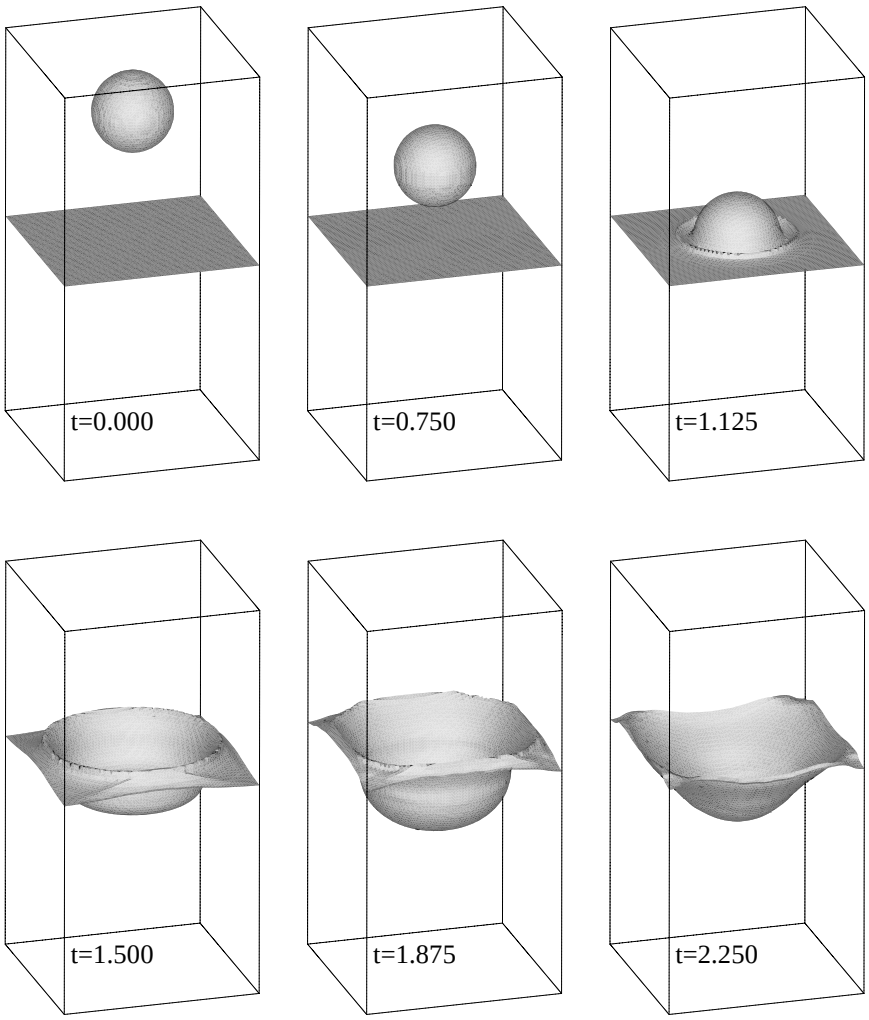

FIG. 11. Three-dimensional falling "droplet" at $Fr = 1$ and density ratio 1000: Iso-surface $\rho = 500$ of density.

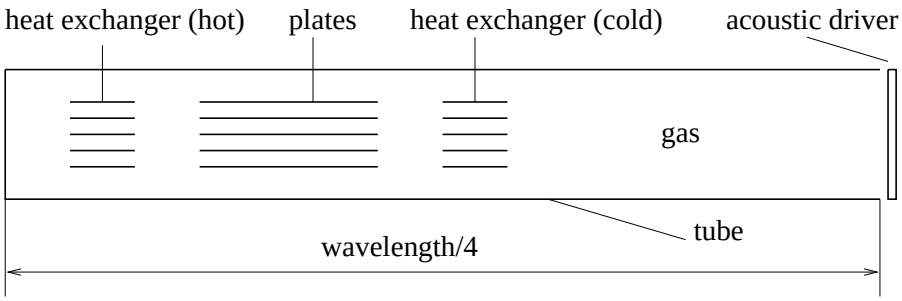

FIG. 12. Sketch of a simplified thermoacoustic refrigerator.

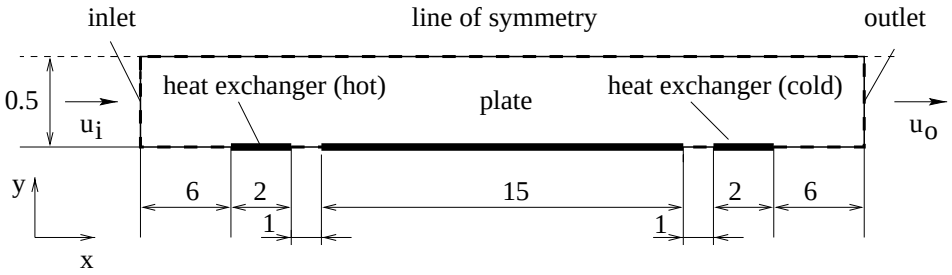

FIG. 13. Computational domain (dotted line).

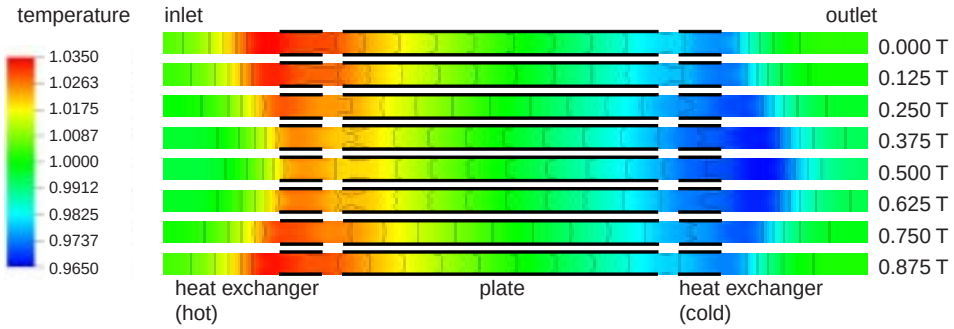

FIG. 14. Temperature field during different times of an acoustic cycle; $T := 2\pi$.

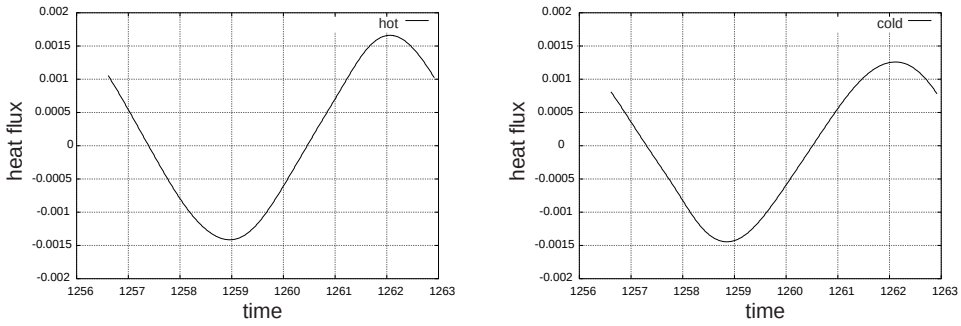

FIG. 15. Heat fluxes through the surface of the hot (left) and cold (right) heat exchanger during an acoustic cycle.

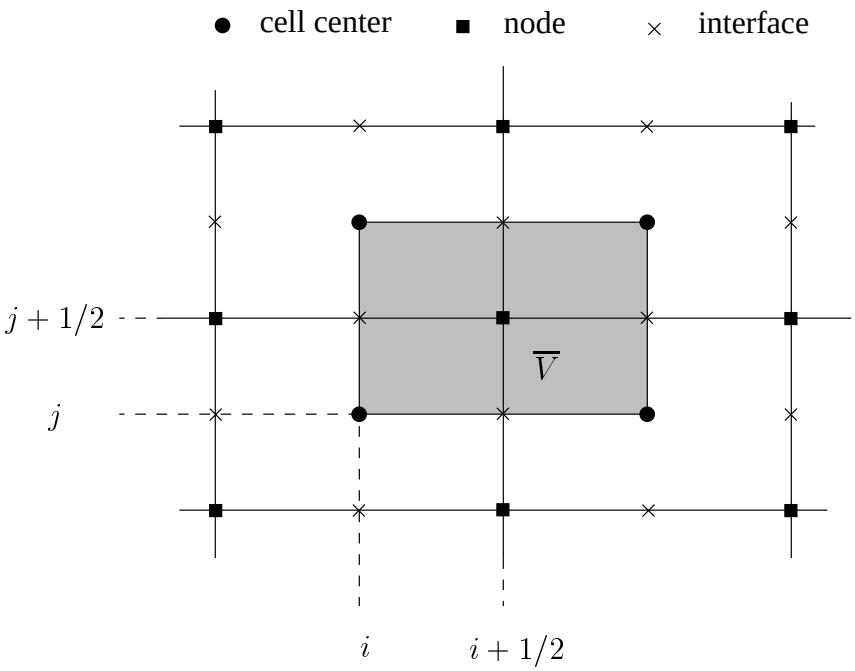

FIG. 16. Two dimensional Cartesian grid.

1. TABLES

TABLE 1

Constant density: errors and convergence rates in the 2-norm and in the maximum norm.

	32×32	rate	64×64	rate	128×128
2-norm	0.193646	2.07	0.0458949	2.10	0.010705
max-norm	0.236456	2.09	0.0553504	2.11	0.012821

TABLE 2

Variable density: errors and convergence rates in the 2-norm and in the maximum norm.

	32×32	rate	64×64	rate	128×128
2-norm	0.229332	2.02	0.0563924	2.16	0.0125899
max-norm	0.263492	1.98	0.0664518	1.68	0.0207160

TABLE 3

Specific number

Pr	0.68	u_{inlet}	$0.7711\cos(t)$
Re	200	v_{inlet}	0.0
γ	$5/3$	u_{outlet}	$1.0267\cos(t)$
T_{hot}	1.0267	v_{outlet}	0.0
T_{cold}	0.9733	λ	0.05
Pe_s	300	κ	41.14